
**Investigation of the Mechanical Tuning for Electron Guns
used in Free Electron Lasers - Finite Element Analysis
of Plastic Deformation and Experimental Validation**

Master's Thesis

in partial fulfilment of the requirements for the degree of

Master of Sciences "M.Sc." in Scientific Instrumentation

Ernst-Abbe-Hochschule Jena
University of Applied Sciences

Department of Sciences and Technology

Scientific Instrumentation

Author:	Sebastian Philipp
Registration-No.:	636564
Academic Supervisor:	Prof. Dr.-Ing. Frank Dienerowitz
Internal Mentor:	Dr. Alexander Donat
Institution's Name:	Deutsches Elektronen-Synchrotron DESY
Date of Submission:	19.12.2014

**Application for the Assignment of the Master's Thesis Topic
for the Degree Programme "Scientific Instrumentation"**

Surname, First Name: Philipp, Sebastian Registration-No. 636564

Email address: sebastian.philipp@desy.de

A Address during Master's Phase:

Kochhannstr. 17, 10249 Berlin

Topic of the Master's thesis:

Investigation of the Mechanical Tuning for Electron Guns used in Free Electron Lasers -
Finite Element Analysis of Plastic Deformation and Experimental Validation

Institution's name: Deutsches Elektronen-Synchrotron Desy

Department: Mechanik

Address: Platanenallee 6
15738 Zeuthen

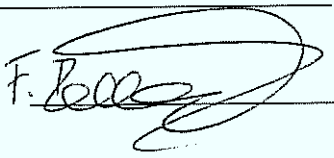
Internal mentor: Dr. Alexander Donat

Signature: 

Phone: 033762 77217

Fax: _____

Academic supervisor: Prof. Dr.-Ing. Frank Dienerowitz

Signature: 

Student's Declaration:

I hereby acknowledge that I am aware of the prerequisites to be met for the assignment of Master's thesis topics under the Examination Regulations of the SciTec Department of the Jena University of Applied Sciences.
Also, I declare that I am not in the process of taking a Master's examination in the same field at any other university or college in the territory to which the German Higher Education Framework Act applies.
Nor is it true that I irrevocably failed a Master's examination in the same subject area at a university or college in the territory to which the German Higher Education Framework Act applies.
I declare that I will observe rules of good scientific practice.

Jena, Zeuthen, 20.08.2014

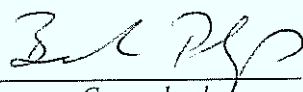
Signature: 
Student

Approval by the course leader Scientific Instrumentation:

Topic approved and assigned on: 2.9.2014

Thesis to be submitted by:
(Approval date + 18 weeks)

6.1.2015

Signature: 
Course leader

Investigation of the Mechanical Tuning for Electron Guns used in Free Electron Lasers - Finite Element Analysis of Plastic Deformation and Experimental Validation

by

Sebastian Philipp

Submitted to the Department of Sciences and Technology
on December 2014, in partial fulfilment of the
requirements for the degree of
Master of Sciences in Scientific Instrumentation

Master's Thesis, Ernst-Abbe-Hochschule Jena 2014, 50 Pages, 52 Figures, 6 Tables,
28 References, 11 Appendices

Abstract

For the operation of free electron lasers (FEL), packages of accelerated electrons are used. At these machines, the first acceleration of the electrons inside the electron gun is essential for the quality of the light produced by the lasers. This acceleration is achieved by the use of a high-frequency electric field, where the dimensions of the electron gun precisely have to match multiples of the wavelength of the field. Therefore, after production the electron gun is tuned by a plastic deformation for which a tuning device is used. During the latest tuning, this device was on its limit and needs to be reviewed.

To calculate the required force for the tuning of the gun, this work presents how plastic deformations can be simulated with the help of the finite element analysis. During the course of this thesis mechanical material data was obtained from material tests and a material model was built within the simulation program ANSYS Workbench. The material model was validated by comparing deformation experiments with their corresponding simulations. Furthermore, an upcoming electron gun was simulated with the help of the obtained material model and an estimation of the load required to tune this gun could be given. This is an important factor for the revision of the tuning device.

Additionally, the deformed shape of the tuned electron gun, that was developed during this thesis, allows to accurately model the electric field within the gun in future work. This helps to further improve the quality of the light emitted by the free electron lasers, which is used in a broad range of experiments in several fields of sciences.

Acknowledgements

I would like to express my gratitude to my supervisor Prof. Frank Dienerowitz for the useful comments and remarks through the learning process of this master thesis. Additionally, in the course 'FEA and Simulations' he gave the basic knowledge for performing the finite element analysis presented in this work.

Furthermore, I would like to thank my internal mentor Dr. Alexander Donat for the intensive discussions on the experiments and the structure of the thesis. I enjoyed writing my thesis under his guidance and encouragement.

Special thanks are due to Niklas Templeton, who helped me a lot in performing experiments and during stimulating discussions supported the organisation of the research.

My sincere thanks also goes to the laboratory for material sciences at the Technische Hochschule Wildau, which gave the permission to use the required equipment to perform the material tests. In particular I would like to thank Ms. Stoycheva, who took time out for supporting the test procedure.

Finally, I would like to deeply thank my family, friends and colleagues, who supported me throughout the entire process of writing the thesis. Here special thanks goes to Hanna Baumgarth, Matthias Philipp and Thomas Jones for proofreading.

Sebastian Philipp

Contents

List of Figures	iii
List of Tables	v
List of Symbols and Abbreviations	vi
1. Introduction	1
1.1. Motivation	1
1.2. Research Objectives	2
1.3. Structure of the Thesis	3
2. Background	4
2.1. Tuning of Electron Guns	4
2.1.1. Tuning Methods	6
2.1.2. Existing Tuning Device	7
2.2. Plasticity of Metals	9
2.2.1. Tensile Test	9
2.2.2. Source of Plasticity	12
3. Material Tests	14
3.1. Specimen Preparation	14
3.2. Tensile Test Procedure	16
3.3. Data Processing and Analysis	18
3.4. Engineering Data in ANSYS Workbench	20
4. Validation of the Plasticity Model	22
4.1. Finite Element Analysis of a Tensile Beam	22
4.1.1. Model Description	22
4.1.2. Results	24
4.2. Experiments on Test Discs	25
4.2.1. Disc Preparation	25
4.2.2. Experimental Set-up	26
4.2.3. Test Procedure	27
4.2.4. Results	28
4.3. Finite Element Analysis of Test Discs	30
4.3.1. Model Description	30
4.3.2. Results	34
4.4. Discussion	36
4.4.1. Comparison of Simulations and Experiments	36
4.4.2. Influences on the Measurements	38
4.4.3. Conclusions	40

5. Finite Element Analysis of the Proposed Gun	41
5.1. Analysis of the Front End	42
5.1.1. Model Description	42
5.1.2. Results	44
5.2. Analysis of the Back Plane	46
5.2.1. Model description	46
5.2.2. Results	47
6. Conclusions and Outlook	49
A. Technical Data Sheets	51
B. Material Data from Tensile Tests	54
C. Detail Views from the Analysis of the planned Gun	56
Bibliography	64

List of Figures

1.1. Comparison of the geometries of Gun 4 and 5	2
2.1. Schematic of the electric field in electron guns	5
2.2. Gun 4 in the tuning device	8
2.3. Tuning device	8
2.4. Typical engineering stress-strain curves	11
2.5. Edge dislocation movement	13
3.1. Dimensions of tensile test specimen	15
3.2. Photo of the tensile test setup	16
3.3. Photo series of a tensile test	17
3.4. Photo of tensile specimens after full tests	18
3.5. Measured engineering stress-strain curves - full range	19
3.6. Measured engineering stress-strain curves - low strain region	19
4.1. Supports and load on the tensile beam	23
4.2. Converged mesh of the tensile beam	24
4.3. Directional deformation of the tensile beam	24
4.4. Drawing of test disc	25
4.5. Experimental set-up for deformation tests	26
4.6. Deformation test of disc 1	27
4.7. Distortion of disc 2	28
4.8. Alignment of force and deformation	29
4.9. Force-deformation curves of test discs	29
4.10. 2D geometry of the test disc for the FEA	30
4.11. Detail view of the supporting edge	31

4.12. Applied boundary conditions for the disc model	31
4.13. Mesh for the test disc	32
4.14. Details of the refined mesh at the disc	32
4.15. Mesh validation for test disc	33
4.16. Stress distribution at the test disc	34
4.17. Stress distribution at the supporting edge	34
4.18. Influence of the geometry of the test discs	35
4.19. Comparison of the tensile test with FEA	36
4.20. Comparison of the deformation of the discs with the FEA	37
4.21. Calibration of the force sensor	38
4.22. Influence of the strain rate	40
5.1. Gun cavity type 5	41
5.2. Simplification on the front end geometry	42
5.3. Location of the applied boundary conditions	43
5.4. Locations of stress singularities	44
5.5. Force-deformation curve of the front end	45
5.6. Reduction of the wall thickness at the front end	45
5.7. Force-deformation curve of the thin front end	46
5.8. Simplification on the back plane geometry	47
5.9. Force-deformation curve of the back plane	48
6.1. Force-deformation curves of the front end	50
C.1. Mesh used for the front end of the gun	56
C.2. Stress distribution at an element size of 1 mm	57
C.3. Stress distribution at an element size of 0.4 mm	58
C.4. Directional deformation of the front end	59
C.5. Directional deformation of the thin front end	60
C.6. Mesh used for the back plane of the gun	61
C.7. Stress distribution at the back plane	62
C.8. Directional deformation of the back plane	63

List of Tables

3.1. Measured dimensions of tensile test specimens	15
3.2. Engineering Data for the FEA-Models	21
4.1. Convergence test of tensile beam mesh	24
4.2. Dimensions of test disc	25
4.3. Convergence test of disc mesh	33
4.4. Influence of the Poisson's ratio	35

List of Symbols and Abbreviations

a	Calibration factor
A_0	Initial cross section area of the tensile specimens
b	Calibration factor
c	Speed of light ($c = 2.998 \cdot 10^8 \text{ m s}^{-1}$)
DESY	Deutsches Elektronen-Synchrotron
E	Young's modulus
\vec{E}	Electric field strength
F	Force
f	Frequency
FEA	Finite Element Analysis
FEL	Free Electron Laser
$F_{tension}$	Applied load during tensile test
\vec{F}	Force acting on a charged particle
L_0	Initial gage length
L_{in}	Initial length before temperature change
OFHC-Copper	Oxygen Free High Conductivity Copper
q	Charge of a particle
RF	Radio frequency
$R_{p0.2}$	Yield strengths at 0.2% strain offset
S	Slip plane
T	Temperature

LIST OF SYMBOLS AND ABBREVIATIONS

t	Time
T_E	Period of the electric field
UHV	Ultra High Vacuum
V_{in}	Input voltage of the force sensor
V_{out}	Output voltage of the force sensor
X	Signal of the force sensor
α	Coefficient of linear expansion
α_{OFHC}	Coefficient of linear expansion for OFHC-Copper
δ	Elongation of the tensile specimens
ε_{app}	Applied strain
ε_{el}	Elastic strain
ε_{eng}	Engineering strain
ε_{pl}	Plastic strain
ε_{tr}	True strain
$\varepsilon_{tr,pl}$	True plastic strain
λ	Wavelength
$\lambda_{OFHC,20^\circ C}$	Thermal conductivity of OFHC-Copper at 20 °C
σ_{app}	Applied stress
σ_{eng}	Engineering stress
$\bar{\sigma}_{eng 3-9}$	Mean engineering stress of specimen 3 to 9
$\sigma_{OFHC,20^\circ C}$	Electric conductivity of OFHC-Copper at 20 °C
σ_{tr}	True stress
σ_u	Tensile ultimate strengths
σ_y	Yield strength
\perp	Position of the dislocation line

1. Introduction

1.1. Motivation

The Deutsches Elektronen-Synchrotron (DESY), by which this master's thesis was hosted, is one of the largest accelerator centres in the world. With the accelerators and detectors developed and built at DESY, it is possible to do fundamental research on particle physics and to use innovative light sources. One type of the light sources provided by DESY are Free Electron Lasers (FELs). At FELs, packages of electrons are accelerated up to a relativistic speed. Under the influence of an alternating magnetic field the electron bunches are deflected to perform a slalom run. At each turn they emit light which is laser like and has a very short wavelength. This light can then be used for a large variety of experiments in several fields of sciences such as biology, chemistry or material sciences [1], [2].

For the quality of the light produced by FELs, the electron emittance in the electron source is essential. The electron sources used at DESY - the so called electron guns - are cavities in which a laser hits a photo cathode to extract electrons. Afterwards, the electrons are accelerated by an alternating electric field with a high field strength [3]. For this, the electric field needs to be in resonance with the cavity which means that the dimensions of the gun cells precisely have to match multiples of the wavelength of the electric field. As it is challenging to manufacture electron guns with the required tolerances, the electron guns are tuned after production. This is done by a plastic deformation of the cavity walls in order to change the length of the cells.

For a better understanding of the plastic deformation during the tuning of electron guns and to be able to estimate the required force for a defined deformation, this work was developed.

1.2. Research Objectives

In order to increase the efficiency of the guns and thereby to improve the quality of the light produced by the FELs, the design of the guns is constantly enhanced. At the moment four types of guns exist and a new type is in the process of planning. Figure 1.1 shows the existing geometry of a gun type 4 in comparison to the geometry proposed for Gun 5.

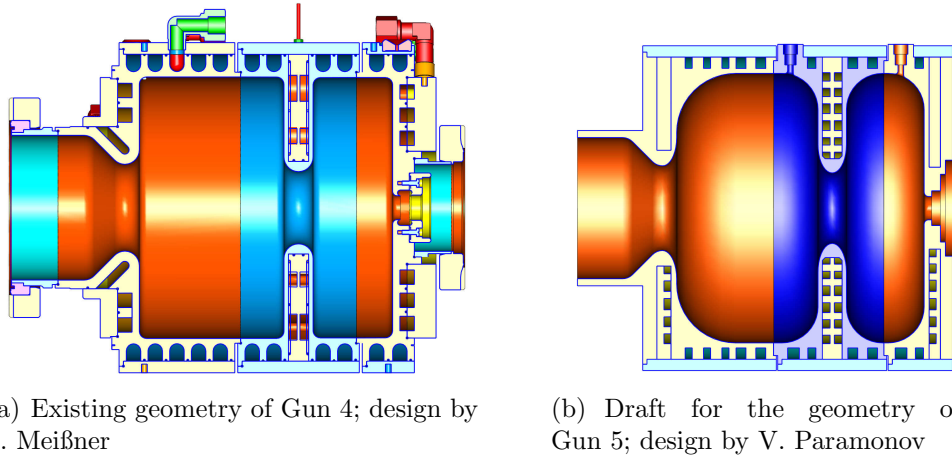


Figure 1.1.: *Comparison of the geometries of Gun 4 and 5*

For tuning the guns, with the help of a tuning device an axial load is applied either at the front or at the back face of the gun. Thereby, the corresponding face is pushed inwards and the cell length is reduced. At the tuning device the load is applied via a gear system, which for the latest tuning of Gun 4 was on its limit [4], [5]. Furthermore, the fillets at Gun 5 are much larger than at Gun 4. Therefore, a higher load for the deformation during the tuning process is assumed.

To review the applicability of the tuning device for the tuning of Gun 5, studies for the plastic deformation using the Finite Element Analysis (FEA) are requested. With the help of the software ANSYS Workbench the required force for a defined deformation of the gun has to be estimated.

For accurate simulations of the plastic deformation, a stress-strain curve of the material to be used in the manufacture of the gun is needed. As in the literature no material data for the special copper of the guns is compiled, material tests are an important part for this work.

Additionally, for the validation of the FEA-model deformation experiments on appropriate test parts are essential.

1.3. Structure of the Thesis

For a general understanding of the tuning of electron guns, Chapter 2 gives the theoretical background, including an approximation for the deformation needed to tune a certain frequency shift. Furthermore, this chapter shows how material data can be developed by a tensile test.

Afterwards, in Chapter 3, the performed tensile tests are described in detail. Here the specimen preparation, the test procedure and the data processing for the use in the FEA software are depicted.

To validate the chosen material model and to verify the finite element analyses, deformation experiments on test discs were performed. Afterwards, their results were compared with the simulation of the same problem. Details of the experiments and simulations are shown in Chapter 4.

In Chapter 5 finite element analyses of the plastic deformation of Gun 5 follows. Here the front end and the back plane of the gun were investigated separately. With the help of the results of the simulations the required force for a defined tuning of the gun was estimated.

Finally, in Chapter 6 all results are summarised and a recommendation for the review of the tuning device is given.

2. Background

For the acceleration of the electron bunches in the electron gun an alternating electric field is used. In order to generate a standing wave of the electric field within the gun, the cavity has to be tuned to a precise cell length. For a better understanding of the influence of the tuning and to estimate the deformation needed to compensate a certain frequency shift, different tuning techniques are described in the first section of this chapter. Furthermore, the tuning procedure used at DESY is depicted.

The second section refers to the material test by which the plasticity of the gun material was analysed. It shows how characteristic values can be obtained, how the data is to be processed for the use in finite element analyses, and which processes enable a plastic deformation of a material.

2.1. Tuning of Electron Guns

Before the tuning techniques will be described, it is explained how the acceleration of electrons in an electron gun works. Figure 2.1 shows a schematic of the electric field distribution in the gun and the position of an accelerated electron bunch for certain times t . Here, T_E is the period of the electric field which can be calculated from its frequency f by $T_E = 1/f$. The nominal frequency of the electric field is 1.3 GHz [6], which is in the range of radio frequency (RF). Therefore, the electric field is often called RF-field.

In Figure 2.1(a) the laser just hit the photo cathode and, by the photo electric effect, several electrons are emitted from it. At this moment the electric field has its highest amplitude. There are two maxima of the electric field strength in the gun. One is located at the cathode surface, where it accelerates the charged electrons in the direction of the gun exit. In Figure 2.1(b) the electrons travelled nearly through the first gun cell. During that, the amplitude of the electric field decreased. However, the spacial distribution of the field maxima stayed the same. As the electron bunch reaches the centre of the gun iris, the electric field becomes zero, as shown in Figure 2.1(c). Thus no further acceleration is applied to the electron bunch. Afterwards, the

electrons enter the second gun cell. In this moment the electric field flips and thus one maximum appears in the centre of that cell (see Figure 2.1(d)). By this field the electrons are further accelerated until they reach the gun exit.

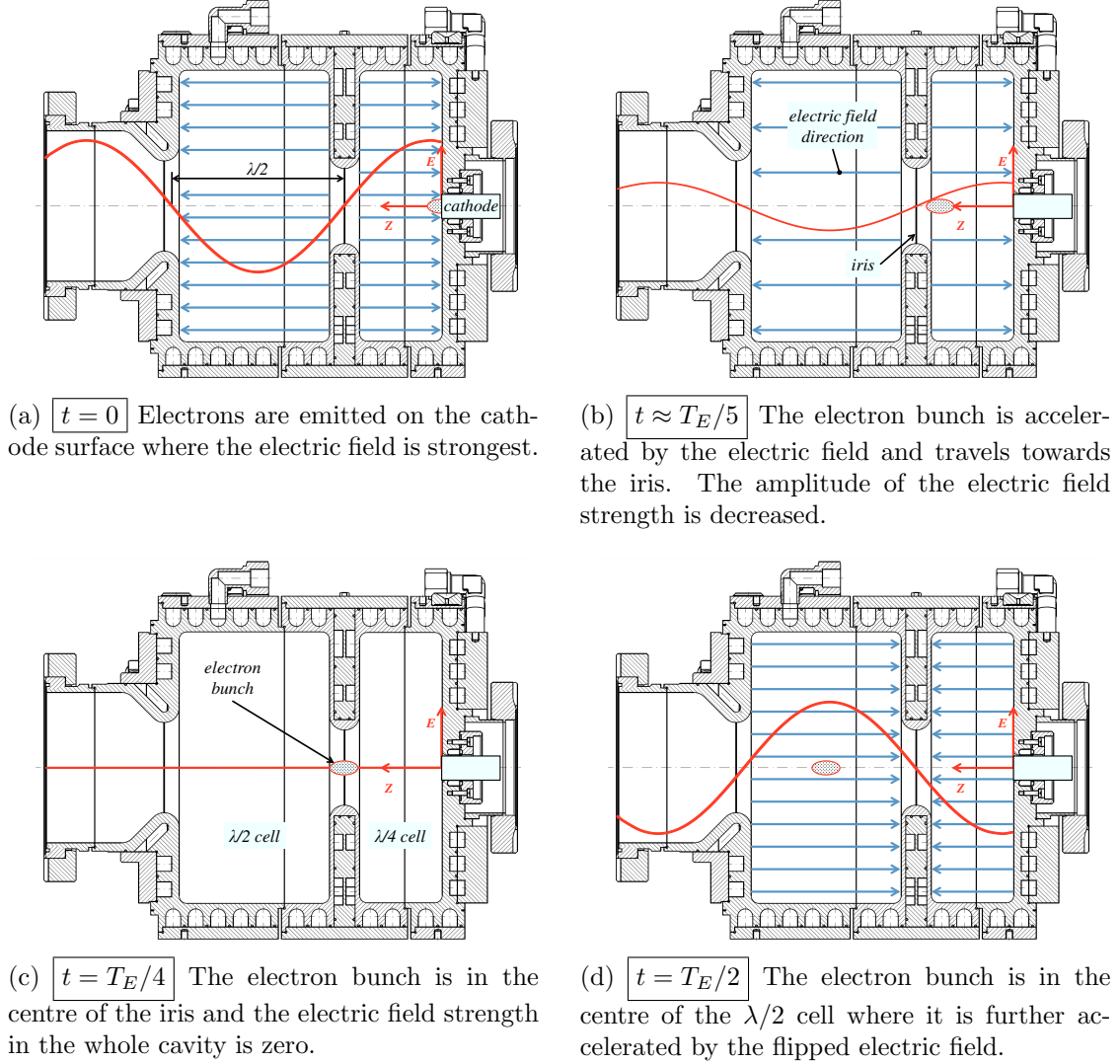


Figure 2.1.: Schematic of the standing wave of the electric field in an electron gun type 4 where the red curve represents the local distribution of the electric field strength $\vec{E}(z)$ on the beam axis and the blue arrows indicate the direction of the electric field

As the electric field strength \vec{E} is defined by the force \vec{F} acting on a particle with the charge q

$$\vec{E} = \frac{\vec{F}}{q} \quad (2.1)$$

and the electrons are charged negative, in Figure 2.1 the electrons are accelerated towards the opposite direction of the electric field.

To achieve a standing wave of the electric field, the cell length of the $\lambda/2$ cell has to fit to multiples of the wavelength λ of the electric field. By Equation 2.2 the relation

between the frequency and the wavelength of an electro magnetic wave in vacuum is given. Here, c is the speed of light, which is about $2.998 \cdot 10^8 \text{ m s}^{-1}$.

$$f = \frac{c}{\lambda} \quad (2.2)$$

Furthermore, to obtain optimum acceleration conditions, the surface of the photo cathode must have a precise position with respect to the electric field maximum in the $\lambda/4$ cell.

During the production of the guns, three main bodies are brazed together to form the two gun cells. This process makes it difficult to match the cell lengths precisely. Hence, the guns have to be tuned in the range of a tenth of a millimetre afterwards.

2.1.1. Tuning Methods

The tuning can be done in two ways: either by a plastic deformation of the gun cell walls or by a temperature change of the gun. Following, the influence of each type of tuning is estimated.

Mechanical Tuning

For the mechanical tuning, the walls of the gun are plastically deformed and thus the wavelength of the standing wave is changed. The frequency shift per wavelength change can be calculated by the first derivative of Equation 2.2, which is

$$\frac{df}{d\lambda} = -\frac{c}{\lambda^2} = -\frac{f^2}{c}. \quad (2.3)$$

With a nominal frequency of $f = 1.3 \text{ GHz}$ it follows

$$\frac{df}{d\lambda} = -\frac{(1.3 \cdot 10^9 \text{ Hz})^2}{2.998 \cdot 10^8 \text{ m s}^{-1}} = -5.64 \cdot 10^9 \text{ Hz m}^{-1} = -5.64 \text{ MHz mm}^{-1}.$$

This means by a 1 mm compression of the $\lambda/2$ cell the resonance frequency is increased by 11.28 MHz. As the deformation accuracy is limited to a few hundredth of a millimetre, this type of tuning is used for rather rough tuning of the guns.

Thermal Tuning

For a finer tuning the thermal expansion of the gun material due to temperature changes is used. Thus, as the temperature T rises, the gun expands and the resonance frequency is shifted to a lower frequency. The material based coefficient of linear expansion α is a measure for the relative change of the length of a material due to a certain temperature change. Following [7] it can be approximated to

$$\alpha = \frac{1}{L_{in}} \cdot \frac{dL}{dT}, \quad (2.4)$$

where dL/dT is the change in length per temperature change and L_{in} is the initial length. By replacing L_{in} with the nominal wavelength λ , for the wavelength change per temperature change it follows

$$\frac{d\lambda}{dT} = \alpha \cdot \lambda. \quad (2.5)$$

Now, by combining Equation 2.3 and 2.5 for the frequency shift per temperature change we get

$$\frac{df}{dT} = \frac{df}{d\lambda} \cdot \frac{d\lambda}{dT} = -\frac{c}{\lambda^2} \cdot \alpha \cdot \lambda = -f \cdot \alpha. \quad (2.6)$$

The inner cells of the electron guns are made of OFHC-Copper, which between 20°C and 100°C has a coefficient of linear expansion α_{OFHC} of $17 \cdot 10^{-6} \text{ K}^{-1}$ [8]. Thus it follows

$$\frac{df}{dT} = -1.3 \cdot 10^9 \text{ Hz} \cdot 17 \cdot 10^{-6} \text{ K}^{-1} = -22.1 \text{ kHz K}^{-1}.$$

For the temperature stability of the guns, a cooling system with water is used. In order to guarantee a fast response of the gun temperature due to a temperature change of the cooling water, the minimum operation temperature lays around 60°C. To avoid any steam in the cooling system the upper operation temperature is limited to 80°C. This gives the possibility for the tuning of several kHz only. However, thermal tuning has the advantage that it can be done during operation.

2.1.2. Existing Tuning Device

For the tuning of the existing electron guns a special device was developed. As shown in Figure 2.2, the gun is fixed between two clamping rings which are connected to a stiff frame. During tuning a load is applied by a thrust bush on a small ring surface on one gun face.

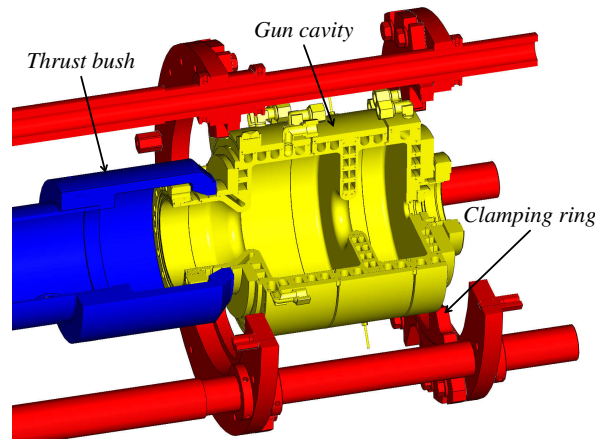


Figure 2.2.: Detail view of Gun 4 in the tuning device during a tuning process; design by C. Martens

Depending on which cell should be tuned the gun can be orientated in the clamping fixture. Under the load the face bends inwards and, when a certain stress is exceeded, it is deformed plastically¹. Thereby, the length of the cell is reduced and its resonance frequency is changed.

Figure 2.3 shows the full tuning device. Here the thrust bush is moved by a spindle gear which can be driven in two ways:

- using a crank handle with direct transmission for a fast motion, or
- using a small hand wheel, whereby a planetary gear produces a high torque with a small travel of the thrust bush.

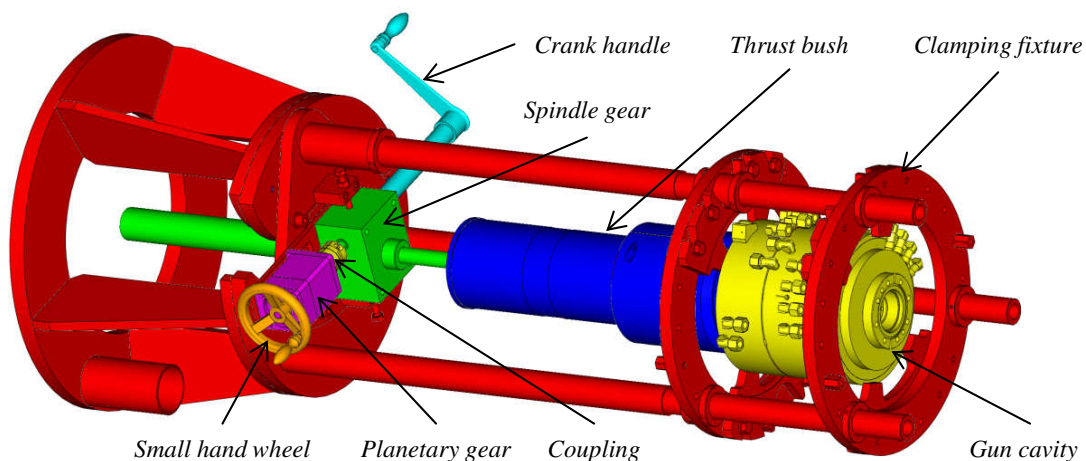


Figure 2.3.: Full tuning device with gear system; design by C. Martens

Thus, the crank handle is used to drive the thrust bush in position and the small hand wheel is used to apply a defined load on the gun surface. To avoid an overloading of

¹This is further described in Section 2.2.

the spindle gear, a flexible coupling between the planetary gear and the spindle gear is used.

For the latest tuning of a Gun 4, a frequency shift of 2 MHz had to be compensated. Thus the $\lambda/2$ cell of the gun had to be plastically deformed by about 0.18 mm. During that, the flexible coupling broke and had to be replaced. However, even after the repair, only by the combined use of the crank handle and the hand wheel it was possible to apply a sufficient load to perform the needed deformation [4], [5].

From the technical data sheets for the coupling and the spindle gear shown in Appendix A, one can conclude that the torque transmitted by the coupling exceeded the maximum torque which could be applied to the spindle gear. The flexible coupling type 300-40 [9] is designed to transmit a torque of 6.5 Nm. As the coupling broke, this torque was exceeded. Furthermore, to the spindle gear type SHG MJ3-L [10] a maximum torque of 5.2 Nm should be applied only. Thus probably a higher torque than recommended was applied to the spindle gear. By this the maximum force of 25 kN, produced by the spindle gear, might be exceeded².

However, for the review of the tuning device with regard to the geometry of Gun 5, the limiting factor is the capability of the spindle gear. Thus, according to Appendix A, the maximum load which can be applied by the tuning device is assumed to be 25 kN.

2.2. Plasticity of Metals

For obtaining mechanical properties of metals, material tests are performed, of which the tensile test is the most important. Following, the test procedure and the obtained results are described. Afterwards, the processes in the inner structure of metals during deformation are depicted.

2.2.1. Tensile Test

With the tensile test it is possible to determine characteristic values like the Young's modulus E , the yield strength σ_y and the tensile ultimate strength σ_u . Furthermore, it delivers information on the strain hardening of a material. These data is essential for simulations of plastic deformation, as it indicates which stress is needed to deform the material by a certain amount.

The standard test procedure is specified by DIN EN ISO 6892 [11]. However, due to

²This might be possible as safety factors are considered usually.

existing licenses the tensile tests described in Chapter 3 were performed according to an old version - named DIN EN 10002 [12]. Nevertheless, for a test procedure where a constant stress rate is used, both regulations show only minor differences (see [13]), that can be neglected. Furthermore, the specimens used for the test can have various shapes but a recommendation is given by DIN 50125 [14].

For the tensile test a specimen with known cross section area A_0 is clamped between two cross-heads of a universal testing machine. Afterwards, an extensometer with an initial gage length L_0 is attached to the specimen. By moving one of the cross-heads, a tensile force $F_{tension}$ is applied to the specimen under which it elongates until it breaks. During the test the elongation of the specimen δ is measured by the extensometer.

Engineering Stress-Strain Curves

To be able to compare material data from tests, where specimens with different shapes were used and to use the data for the calculation of the deformation of a component under a certain load, the parameters engineering stress σ_{eng} and engineering strain ε_{eng} are used. A stress is a measure of an internal force acting perpendicular to a certain area in the material and a strain represents a relative elongation. Both - engineering stress and strain - can be derived from the tensile test by

$$\sigma_{eng} = \frac{F_{tension}}{A_0} \quad (2.7)$$

and

$$\varepsilon_{eng} = \frac{\delta}{L_0}. \quad (2.8)$$

With the help of these parameters it is possible to draw an engineering stress-strain diagram, in which every material shows a characteristic curve. In Figure 2.4 the engineering stress-strain curves for two different materials are plotted.

Both material curves start with a linear part in which the materials behave elastic - meaning by a stress relief the materials go back in their original shape. The slope of the stress-strain curve in this region is called Young's modulus E , which links the engineering stress with the engineering strain by the Hooke's law:

$$\sigma_{eng} = E \cdot \varepsilon_{eng}. \quad (2.9)$$

After a certain elongation, the materials deviate from this linear proportionality and show a plasticity - thus by a stress relieve the materials stay partial deformed. As shown

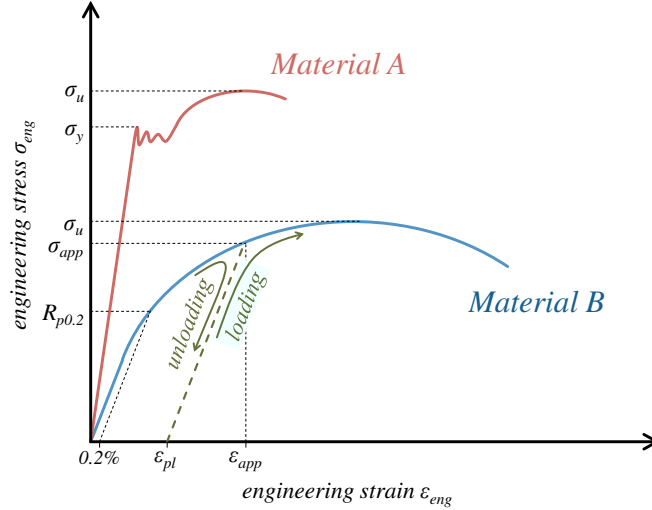


Figure 2.4.: Typical engineering stress-strain curves for a material with distinct yield strength (material A, e.g. structural steel) and a material with indistinct yield strength (material B, e.g. copper)

on the stress-strain curve of Material B in Figure 2.4, the remaining plastic strain ε_{pl} after unloading can be obtained by drawing a line with the slope of the Young's modulus through the point of the highest applied stress σ_{app} . At the intersection of this line with the strain axis one can read the remaining plastic strain. If the material is reloaded up to the earlier applied stress, it behaves elastic and if the stress is further increased it shows further plasticity. Thereby, the elastic region is extended which is called *strain hardening*.

The plastic strain at a certain applied stress can be calculated by subtracting the elastic strain ε_{el} from the applied strain ε_{app} . Thus it follows

$$\varepsilon_{pl} = \varepsilon_{app} - \varepsilon_{el} = \varepsilon_{app} - \frac{\sigma_{app}}{E}. \quad (2.10)$$

However, at the tensile test the specimens are stretched till they break. Thereby, the engineering stress-strain curves of metals show a maximum in stress which is denoted as tensile ultimate strength σ_u . This is the highest stress that can be applied to a component if it is allowed to deform plastically. Afterwards, necking starts at one point of the specimen and for a further elongation a lower tensile force is needed. Thus, as in Equation 2.7 the cross section area is assumed to be constant, the engineering stress decreases till the specimen breaks abruptly.

Some metals, like Material A in Figure 2.4, have a distinct elastic limit at which the stress is called yield strength σ_y . In most engineering applications the highest stress, allowed within a component, is a fraction of the yield strength. This guarantees that the components are not deformed plastically. For materials with a stress-strain curve

like the one of Material B in Figure 2.4, the elastic limit can not be pinpointed as easily. Therefore, the yield strength at 0.2% strain offset $R_{p0.2}$ is often used, to limit the elastic region [15], [16], [17] and [18].

True Stress-Strain Curves

So far, for calculating the stress in the tensile specimen it is assumed that its cross section area stays constant. However, this is not true as the volume of the specimen does not change and therefore, an extension leads to a reduction of its cross section area. To consider this, according to [17] and [19] the true stress σ_{tr} , acting within the specimen, can be calculated by

$$\sigma_{tr} = \sigma_{eng} (1 + \varepsilon_{eng}) . \quad (2.11)$$

Furthermore, in Equation 2.8 the strain refers to the initial gage length. Though, as the specimen expands, the increment of strain is based on the current length of the specimen. Therefore, according to [17] and [19] its true strain ε_{tr} is calculated by

$$\varepsilon_{tr} = \ln (1 + \varepsilon_{eng}) . \quad (2.12)$$

Additionally, to insert the material data from a tensile test into the simulation software ANSYS Workbench, the user has to provide a data set of true stress versus true plastic strain. In analogy to Equation 2.10 the true plastic strain $\varepsilon_{tr,pl}$ can be calculated by:

$$\varepsilon_{tr,pl} = \varepsilon_{tr} - \frac{\sigma_{tr}}{E} . \quad (2.13)$$

2.2.2. Source of Plasticity

To understand what happens during the deformation of a metal, its inner structure needs to be considered. All metals consist of crystalline lattices, where atoms are arranged in a long-range order. Volumes in which a lattice is orientated in one direction are called grains. As it is not possible to produce a perfect crystalline structure, all metals exhibit defects in their lattice. These imperfections significantly affect the properties of the metal and can be classified under four divisions: point defects, line defects, planar defects and volume defects [16].

The most important defect for the plasticity of a metal is called edge dislocation, which belongs to the group of line defects. Figure 2.5 schematically depicts such

an edge dislocation, at which an extra plain of atoms is present above a dislocation line. The dislocation line is indicated by the symbol \perp . This extra plain of atoms forces the neighbouring atoms to be pushed out of their equilibrium position, shown in Figure 2.5(a).

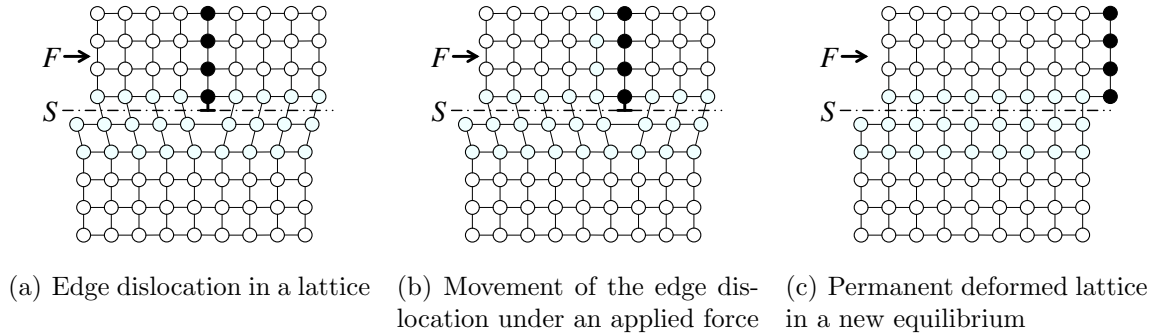


Figure 2.5.: *Edge dislocation movement in a crystalline lattice, adapted from [16]*

If now a force F is applied to the lattice, the additional atoms can establish bonds with atoms below the dislocation line and replace their neighbouring atoms. Thereby, the edge dislocation is moved by an inter-atomic distance, depicted in Figure 2.5(b). This is repeated over the whole grain until the edge dislocation reaches the grain boundary and the dislocation line forms a plane, on which the upper atoms slip, called slip plane S . Thereby, the lattice is permanently deformed, as shown in Figure 2.5(c).

Thus, only single bonds are broken at one time, rather than all bonds in the slip plane at once. Due to the present of dislocations a plastic deformation can occur at much lower stresses than at a perfect crystalline structure.

However, during cold forming of a metal additional edge dislocations are formed. By these additional defects, the movement of the edge dislocations is hindered and higher stresses are needed, for a further deformation. This is the above mentioned strain hardening.

If afterwards the metal is annealed at temperatures above its recrystallisation temperature, new grains with less defects are formed. Thereby, the strain hardening effect is eliminated and the metal becomes as soft as before cold forming [15], [16] and [20].

3. Material Tests

This chapter describes the preparation of the tensile test specimens, the procedure of the tensile test and the processing of the measured data to be able to use them for the simulations.

The existing gun cavities are made from Oxygen Free High Conductivity Copper (OFHC-Copper). This copper is more or less free from any additives and has a very low oxygen content (less than 0.001%). The material is chosen as it shows a high electric and thermal conductivity ($\sigma_{OFHC,20^\circ C} = 59 \cdot 10^6 \text{ S m}^{-1}$ and $\lambda_{OFHC,20^\circ C} = 393 \text{ W m}^{-1} \text{ K}^{-1}$ [8]) which is needed for a fast distribution of the heat induced by the alternating electric field in the gun.

Furthermore, due to the low oxygen content OFHC-Copper is the only type of copper to be used for vacuum applications. As opposed to standard copper, there is hardly any oxygen available which during baking could react with hydrogen from the atmosphere to form water. Such reaction at normal copper leads to cracks in the material which is called *steam embrittlement* and produces vacuum leaks. Additionally, OFHC-Copper is free from evaporating elements and thus pressures in the Ultra High Vacuum (UHV) region can be reached. Therefore, OFHC-Copper is chosen if it comes to vacuum applications where copper is needed [15], [21].

To simulate plastic deformation with the FEA-software ANSYS Workbench one needs to provide a stress-strain curve of the used material. For OFHC-Copper it is difficult to find such material data in the literature, especially as during production the guns are brazed and thereby the copper is annealed. Therefore, it was decided to perform tensile tests to obtain a stress-strain curve which afterwards was used in ANSYS Workbench.

3.1. Specimen Preparation

For the material tests a 6.35 mm thick OFHC-Copper plate was available at DESY. From it the profile of nine tensile test specimens and three test discs (see Section 4.2) were wire eroded. According to the specimen specification [14] the recommended

dimensions for flat specimens are shown in Figure 3.1.

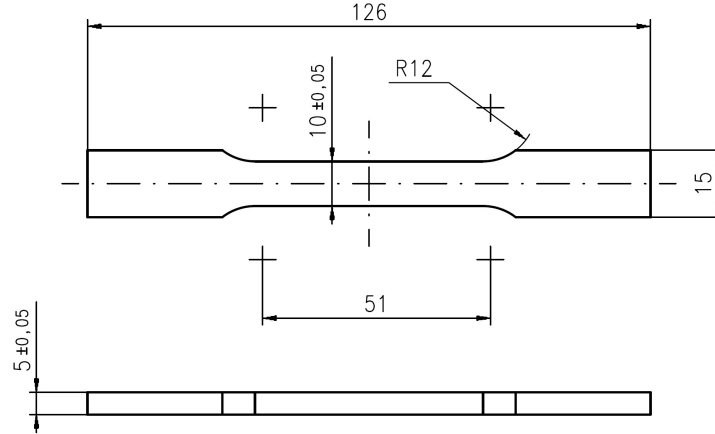


Figure 3.1.: *Dimensions of the used tensile test specimen according to [14]*

After wire eroding the specimens should have been milled to a thickness of 5 mm. Unfortunately, due to time restrictions for the following annealing process only two specimens were fully machined. The rest were machined from one side only. By that the initial cross section areas A_0 of the different specimens varied in a bigger range as planned, shown in Table 3.1. However, according to the test specification [12] other cross section areas than recommended in [14] are allowed but their cross section areas have to be considered for the calculation of the engineering stress σ_{eng} .

Table 3.1.: *Measured dimensions of tensile test specimens after full machining and annealing*

Number	Hight / mm	Width / mm	A_0 / mm ²	Machining
1	5.56	9.95	55.32	one side
2	5.58	9.95	55.52	one side
3	5.25	9.97	52.34	one side
4	5.94	9.97	59.22	one side
5	4.98	9.97	49.65	both sides
6	6.04	9.96	60.16	one side
7	4.95	9.98	49.40	both sides
8	5.68	9.97	56.63	one side
9	5.65	9.97	56.33	one side

Furthermore, during brazing of the electron guns the OFHC-Copper is annealed and thereby becomes softer than the cold worked plate from which the specimens were made. Therefore, to obtain the same material properties, after machining the tensile test specimens and the test discs were annealed at about 850 °C in a vacuum furnace. During the brazing process of the electron guns the temperature of the solder is monitored to control the temperature regime. Therefore, it was decided to anneal the probes

during the brazing of a vacuum part with similar size and geometry as an electron gun [22]. Thus one can assume that the probes had the same material properties as the copper of a brazed electron gun.

3.2. Tensile Test Procedure

The tensile tests were performed in the laboratory for material sciences at the Technische Hochschule Wildau. There, a universal testing machine by Zwick was available which can apply a maximum load of 20 kN. As a hardening over time was observed at existing parts made of annealed OFHC-Copper, two test dates were agreed: one about 65 hours after the annealing process and a second one 7 weeks later. On the first test date specimen 1 to 5 and the second specimen 6 to 9 were tested.

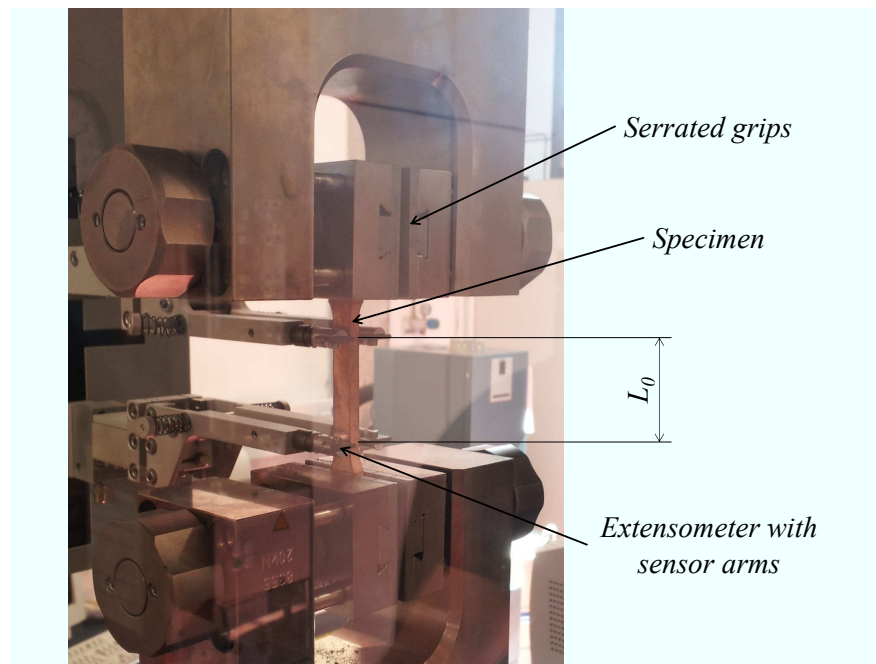


Figure 3.2.: Photo of the universal testing machine with installed specimen

For the tests, the shoulders of each specimens were clamped between serrated grips in the testing machine as shown in Figure 3.2. The clamping force was applied with the help of a spanner at which the fastening torque could not be measured. However, after the first specimen slipped before fracture, it was decided to use the highest force which could be applied with the given spanner. After clamping, the tension force sensor of the testing machine was zeroed and the dimensions of the specimens were entered in the control software of the testing machine. Thereby, a constant stress rate of 10 MPa s^{-1} could be guaranteed as recommended by [12]. To measure the elongation of the specimens an extensometer with sensor arms was used, where the initial gage

length L_0 was set to 40 mm.

During the tests the lower mount of the testing machine was driven downwards thus tension was applied to the specimens. Due to the tension the specimens were elongated and by that their cross section areas were reduced. After a certain elongation necking occurred at one point of the specimens which after further elongation caused the fracture of the probe. The whole process is shown in Figure 3.3. During the tests the applied force and the elongation of the specimens were recorded.

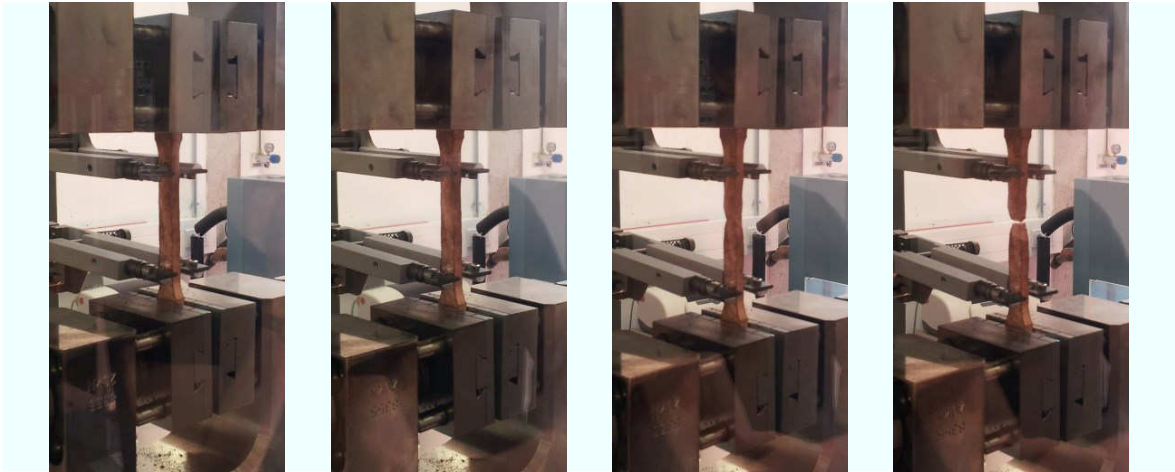


Figure 3.3.: *Photo series of the tensile test on specimen 4*

During the tests the following was observed or changed:

- The clamping force was not sufficient for the first test and therefore the serrated grips slipped just before necking began.
- On specimen 2 the necking occurred outside the gage length covered by the extensometer.
- To test the influence of the clamping, grips with higher roughness were used for the last test.
- During all tests the smooth machined surfaces of the specimens became rough and bumpy.

Figure 3.4 shows all specimens after the tensile tests were performed. The different lengths after fracture correspond to the different cross section areas of the specimens. Furthermore, it shows that the position, where necking arose and the specimen finally failed, is randomly distributed and can not be predicted.



Figure 3.4.: *Photo of all tensile specimens after the tests were performed*

3.3. Data Processing and Analysis

After all tensile tests were finished, for each specimen the applied load and the elongation were transformed into engineering stress and engineering strain. Therefore, Equations 2.7 and 2.8 were used with an initial gage length L_0 of 40 mm and the initial cross section areas A_0 from Table 3.1. Thereby, the engineering stress-strain curves shown in Figure 3.5 and 3.6 could be plotted.

In the first diagram for specimen 1 the sharp decrease of stress with no further increase in strain corresponds to the slipping of the clamps. Due to the slipping, the load on the specimen was removed abruptly and the specimen contracted by the elastic strain. Therefore, after the highest stress the engineering stress-strain curve shows a straight line with the slope of the Young's modulus.

For specimen 2 the stress-strain curve also shows a sharp decrease of stress. This corresponds to the fact that the necking occurred outside the gage covered by the extensometer. As a result, the elongation in the necking region was not measured and could not be added to the strain. Furthermore, due to the reduced cross section area caused by the necking, the engineering stress decreased. Additionally, it is recognisable that the tensile yield strength for this specimen is slightly higher than for all others.

As depicted in Figure 3.5, the tensile ultimate strengths σ_u for all specimens are between 210 MPa and 230 MPa. From Figure 3.6 the Young's modulus E can be estimate to be 90 GPa. By a parallel shift of the straight line with the slope of the Young's modulus one can read the yield strengths at 0.2 % strain offset $R_{p0.2}$ which lay between 24 MPa and 35.5 MPa¹.

¹Except specimen 2 where $R_{p0.2}$ is about 47 MPa.

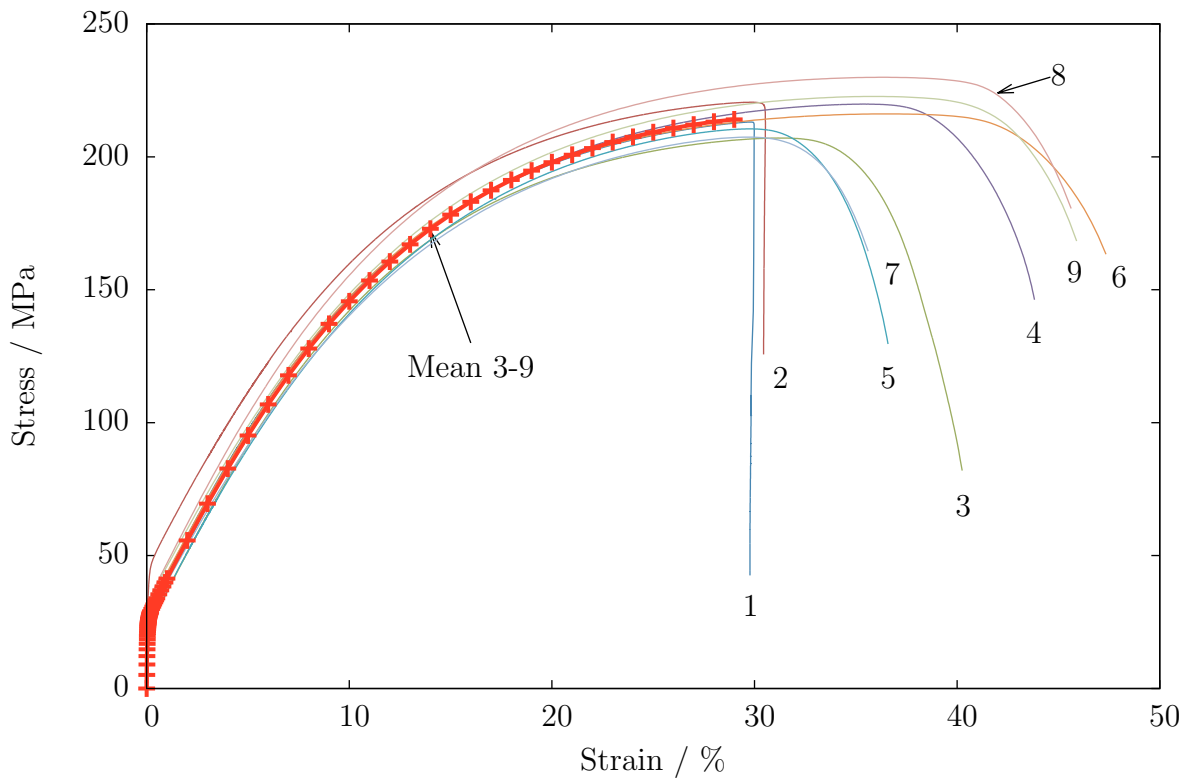


Figure 3.5.: Full engineering stress-strain curves of the nine tensile tests with mean curve averaged from specimen 3 to 9

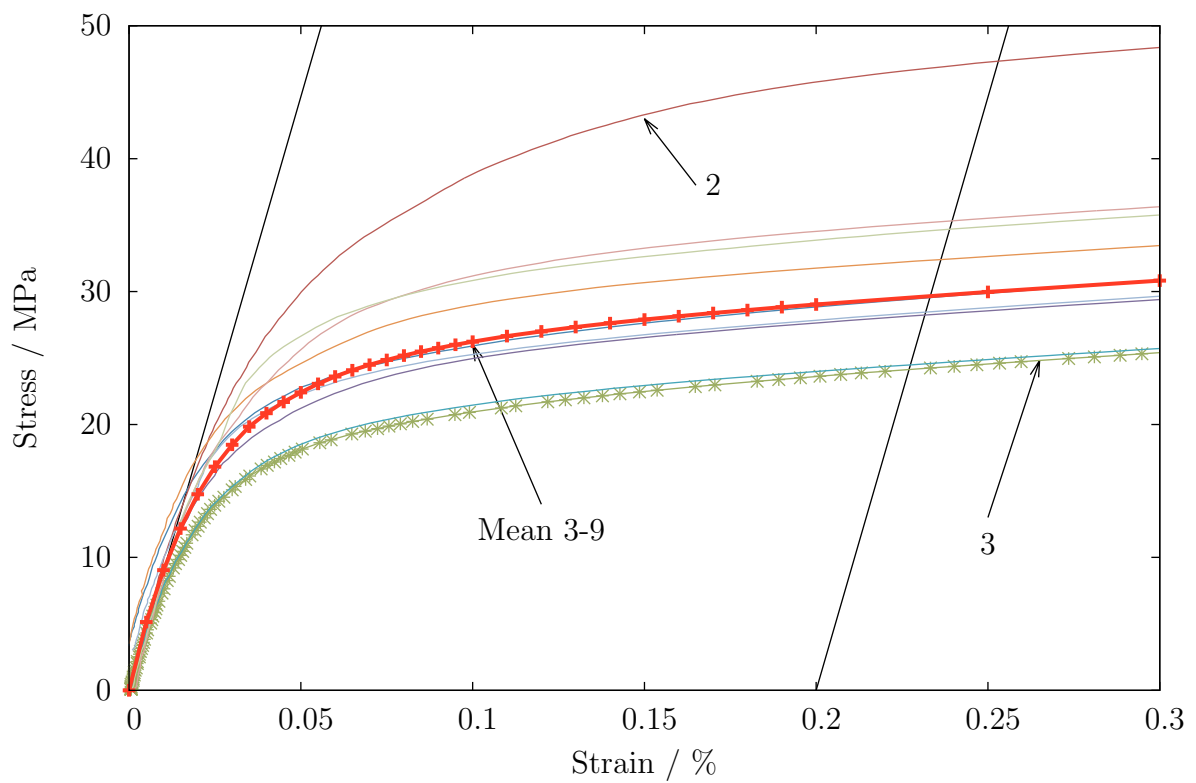


Figure 3.6.: Low strain region for the engineering stress-strain curves of the nine tensile tests with mean curve averaged from specimen 3 to 9

Additionally, the different stress-strain curves indicate that the ageing had no effect on the mechanical material properties of the OFHC-Copper. Specimen 1 to 5 were tested shortly after the annealing. They should show a lower tensile yield strengths and a lower tensile ultimate strengths than specimen 6 to 9, which were tested seven weeks later. As shown in Figure 3.5, there was only a small spreading of the stress-strain curves. This is expected for material tests and therefore no hardening over time could be noticed.

For the data input in ANSYS Workbench, the user needs to provide a data set of true stress versus true plastic strain. To be able to calculate this data, the engineering stress-strain curves of the tensile tests were combined to a mean engineering stress-strain curve. Due to the irregularities during the tests of the first two specimens, only the data for specimen 3 to 9 were included in the mean curve. Therefore, the stresses at certain strains² were interpolated for each specimen. Afterwards, for every strain step, the stresses of the specimens were averaged to the mean stress $\bar{\sigma}_{eng3-9}$. The mean stress-strain curve is plotted in Figure 3.5 and 3.6.

In ANSYS Workbench the input data to build the $\sigma_{tr} - \varepsilon_{tr,pl}$ curve is limited to 101 data sets. Therefore, in regions with low gradients the interpolation width for the stresses were chosen wider than in the original data. To illustrate this, in Figure 3.6 the stress-strain curve for specimen 3 and for the mean curve are plotted with their data points. However, the reduced data does not lead to a significant loss of material information.

From the mean engineering stress-strain curve the true stress-strain curve was computed by the use of Equations 2.11 and 2.12. To calculate the true plastic strain, Equation 2.13 was used. The obtained data are shown in Appendix B. Furthermore, for the multilinear isotropic hardening model the input data need to start with the true stress up to which Hooke's law is valid, which is the stress up to which the material behaves perfectly elastic. Therefore, as for the first three points the plastic strain is zero, the first two points are not needed in ANSYS Workbench and were cancelled out.

3.4. Engineering Data in ANSYS Workbench

To insert the stress-strain curve for OFHC-Copper in the ANSYS model, a new material was defined in the Engineering Data. For this, properties of isotropic elasticity were added to the material as shown in Table 3.2.

²See Appendix B for the full list.

Table 3.2.: *Engineering Data for OFHC-Copper and stainless steel used for the finite element analyses*

Property	OFHC-Copper	Stainless steel
Young's modulus / GPa	90	193
Poisson's ratio	0.34	0.31
Yield strength / MPa		207

Here, the Young's modulus is a result of the tensile test (see Section 3.3). As the Poisson's ratio was not measured and is not defined by [8], the value of the copper alloy, given in the general materials in the Engineering Data sources of ANSYS Workbench, was used. However, as shown in Section 4.3.2, the Poisson's ratio has only a small influence on the simulations and therefore does not play a critical role.

As the next step a multilinear isotropic hardening model was added to the material. This model was chosen, as according to the ANSYS training material [19], it is the most suitable material model for simulations of large strain. In the model the user is asked to fill a table of plastic strain versus stress. According to [19], at this point data of true plastic strain versus true stress have to be provided. Thus the data shown in Appendix B were added.

However, as all specimens were made from the same plate, the test does cover one batch of production only. Thus for other OFHC-Copper plates the material data may differ. Furthermore, the material is assumed to be homogeneous. This might not be quite correct as the stress-strain curves did spread. To compensate this spreading, the curves were averaged. Though, for evaluating the results of a FEA one has to consider that the real material may behaves slightly different.

Furthermore, in the models described in Section 4.3 and Chapter 5, some parts are made from stainless steel. Therefore, from the general materials in the Engineering Data sources of ANSYS Workbench stainless steel was added to the model. Its material data are shown in Table 3.2.

4. Validation of the Plasticity Model

To ensure that the insights gained from simulations can be applied to the real world problems, FEA-models are verified by experiments or at least by a hand calculation of a simplified model. As the calculation of plastic deformations is challenging, it was decided to perform deformation experiments to validate the chosen material model.

In this chapter, first the simulation of one tensile specimen is described. Afterwards, the test procedure for deformation experiments on three test discs is shown. These experiments were then modelled within ANSYS Workbench. Finally, all results are summarised and conclusions are drawn for the simulation of Gun 5 presented in Chapter 5.

4.1. Finite Element Analysis of a Tensile Beam

To verify the material model, in a first validation step the tensile test was simulated. Therefore, on a simple beam with the dimensions of one of the specimens, a tensile force was applied. As the force and deformation from the real tensile test, presented in Chapter 3 are known with a good accuracy, the results of the finite element analysis were compared with the measured data. Furthermore, due to the simple shape of the beam a coarse mesh could be used. Thus, the computational effort was very low and adjustments could be tested rather fast.

4.1.1. Model Description

As the measured stress-strain curve of specimen 4 is closest to the mean stress-strain curve (see Figure 3.5), it was decided to model a simplified tensile beam with the same cross section. Thus, according to Table 3.1, a 5.94 mm by 9.97 mm rectangle was drawn in the Design Modeler of ANSYS Workbench. As the extension of the specimen was measured with a gage length of 40 mm, the rectangle was extruded by that length afterwards.

The tensile test was performed under a non-alternating load and thus for its simulations it was decided to use the Static Structural tool within ANSYS Workbench. In it the material data of OFHC-Copper from Section 3.4 were assigned to the geometry and nonlinear effects were switched on.

During the tensile test the specimen is stretched in one axis and compressed in the two others. To enable the tensile beam to behave in the same way, only one corner was fixed. Additionally, a frictionless support was applied to the back face of the tensile beam as shown in Figure 4.1. To disable a rotation around the fixed corner, the displacement of the edge marked with C in Figure 4.1 was fixed in Y and Z direction but kept free in X direction. Furthermore, a force of 12600 N was applied to the face opposite the frictionless support. This value was chosen as at this load the calculated engineering stress in the specimen was just below the highest stress of the mean curve. Additionally, large deflection was switched on in the solver controls of the analysis settings.

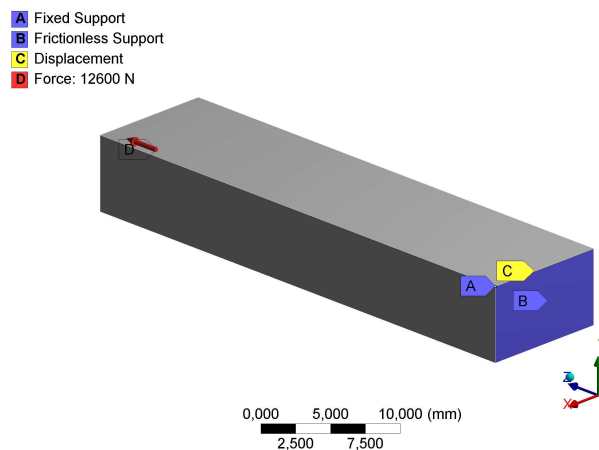


Figure 4.1.: Locations of the supports and the load applied to the tensile beam

Figure 4.2 shows the converged mesh of the tensile beam. It was defined by a coarse relevant centre and an element size of 5 mm. Thus, 32 elements of the type SOLID186 were built. According to the ANSYS help [23], this type is a higher order 3D 20 node solid element, which exhibits quadratic displacement behaviour. Furthermore, it supports plasticity, large deflection and large strain capabilities.

To prove that the mesh is suitable for the model, a convergence test was done. For this, changes of the maximal deformation in Z direction and maximal overall stresses were examined for different element sizes. As shown in Table 4.1, for the reduced element sizes the investigated results did not change. This is based on the simple shape of the beam which can be well represented by the elements. Thereby, the use of elements with a size of 5 mm was verified.

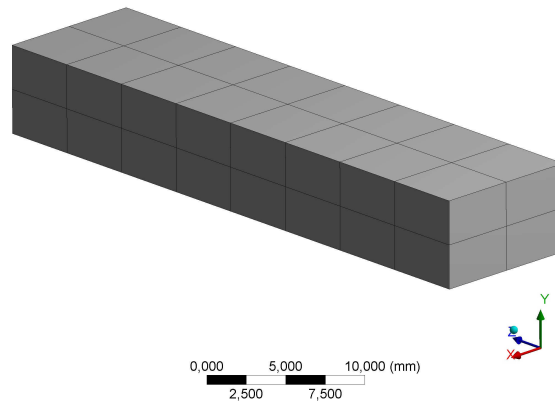


Figure 4.2.: Converged mesh of the tensile beam

Table 4.1.: Convergence test of the mesh of the tensile beam

Element size / mm	Number of nodes	Directional deformation max. / mm	Stress max. / MPa
5	261	10.958	270.78
2.5	1187	10.958	270.78
1	11813	10.958	270.78

4.1.2. Results

Figure 4.3 shows the deformation of the tensile beam in Z direction with the wire frame of the undeformed beam. Here, it is clearly evident, that the cross section of the deformed beam is equally reduced over the whole length. Thus the boundary conditions were applied correctly. Furthermore, the maximum deformation in the direction of the load is 10.958 mm.

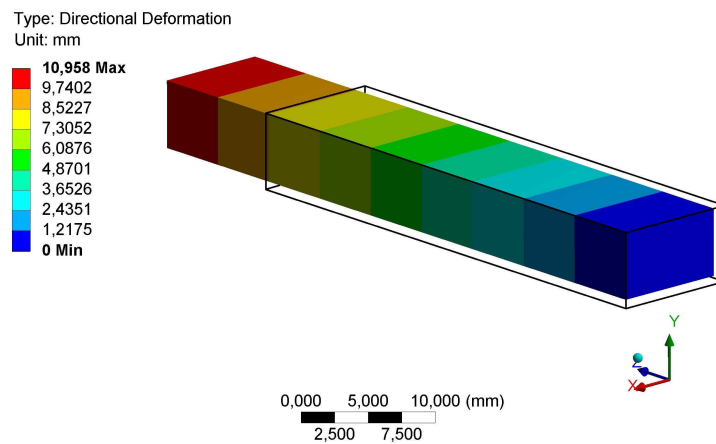


Figure 4.3.: Directional deformation of the tensile beam in mm; depicted in true scale with respect to the undeformed beam shown as wire frame

Additionally, under the highest load a stress of 270.78 MPa acts equally over the entire beam. As there are no stress maxima, it further confirms that the boundary conditions were applied correctly.

4.2. Experiments on Test Discs

As the specimens were not unloaded during the tensile test, it was not possible to measure the fraction of plastic strain from the overall strain. To evaluate this and to test the simulations on a more complex part, three test discs were manufactured from the same copper plate as the specimens. Afterwards, the discs were deformed under a mechanical press. During that, force and deformation were measured. These measurement results helped to validate the FEA-simulations of the same disc.

4.2.1. Disc Preparation

As mentioned in Section 3.1, the outer diameters of the test discs were wire eroded from the same 6.35 mm thick OFHC-Copper plate as the tensile test specimens. Afterwards, as the thickness of the copper plate was not constant over the full area, it was decided to machine all discs from both sides to guaranty parallel faces. Thereby, the thickness of the discs varied as shown in Table 4.2. Additionally, the recess shown in Figure 4.4 was machined on each disc.

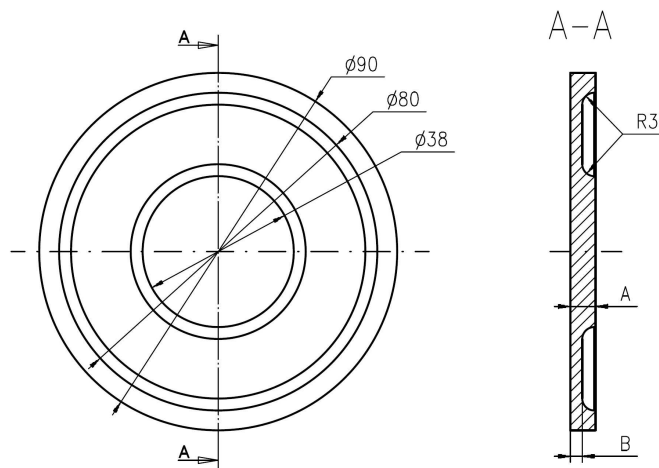


Figure 4.4.: Drawing of test disc

Table 4.2.: Designed and measured values for the variables A and B in Figure 4.4

	$A /$ mm	$B /$ mm
Designed	6.35	3
Disc 1 & 3	5.83	2.95
Disc 2	5.6	2.65

After all discs were fully machined, they were annealed together with the tensile specimens. Thus it can be assumed that the discs had the same materials properties as the tensile specimens.

4.2.2. Experimental Set-up

After annealing, the test discs were deformed with the help of a spindle press. For this, the experimental set-up shown in Figure 4.5 was used. Here, the ram of the press applied a load to a force sensor which was placed on top of the test disc. Thus, the force transmitted by the force sensor was measured. For surveying the deformation of the disc, a length gauge was attached to the bottom of the disc with the help of a mounting device. The spacer ring, shown in Figure 4.5, was only used for the tests of disc 3. It was inserted after disc 2 crashed into the bolster plate of the press.

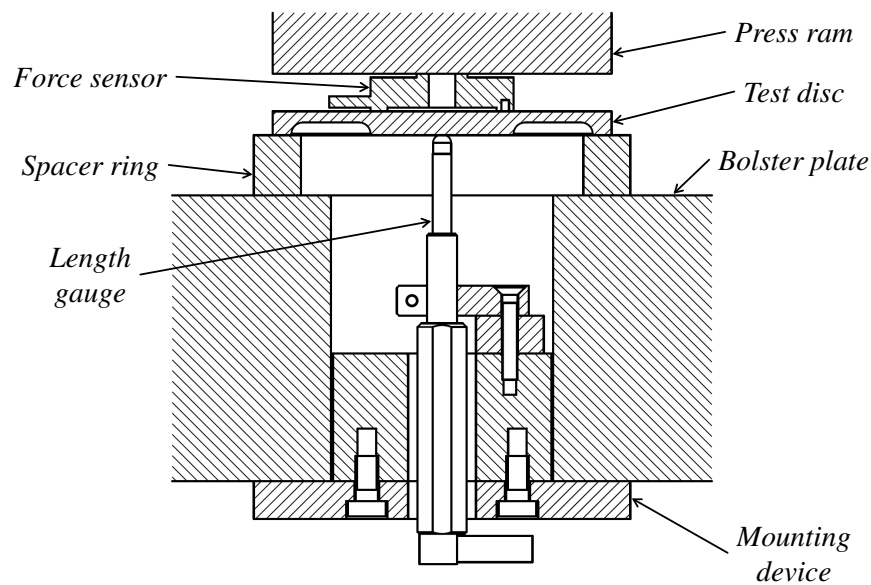


Figure 4.5.: *Experimental set-up for the deformation of the test discs*

Due to the recess in the disc, it was expected that the surface of its centre part would only exhibit a small curvature after deformation. Thereby, for measuring the maximum deformation of the test disc, the alignment of the length gauge and the disc was not critical.

To measure the load applied to the test discs, a force sensor type KM38 20kN [24] was used. It can measure forces up to 20 kN. For this a direct voltage of 10 V, provided by a laboratory power supply, was applied to a bridge circuit inside the sensor. As the force acting on the sensor changed, the resistance of one resistor within the bridge circuit was modified. Thereby, the output voltage of the bridge circuit changed proportional. Thus, by taking the ratio between the output and input voltage and multiplying it with a calibration factor, it was possible to determine the applied force. Both voltages were measured by a data acquisition unit type 34970A with a 20-channel multiplexer

plug-in module type 34901A [25]. The data acquisition unit took simultaneous readings of both voltages every quarter of a second.

For the measurement of the deformation of the test discs, an incremental length gauge type ST 1288 [26] was used, which was connected to an evaluation unit type ND 2100G GAGE-CHECK [27]. The length gauge had a measuring range of 12 mm with an accuracy of $\pm 1 \mu\text{m}$. Furthermore, the evaluation unit took readings of the deformation every third of a second approximately.

4.2.3. Test Procedure

First disc 1 was deformed by slightly more than 3 mm. To avoid a lifting of the disc caused by the spring implemented in the length gauge, the disc was fixed by two clamps as shown in Figure 4.6. However, as these clamps were hand tighten only, they did not have a major influence on the deformation of the disc.

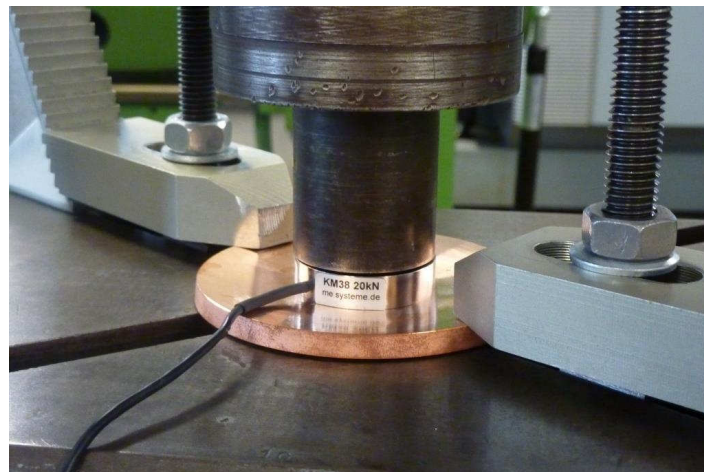


Figure 4.6.: *Deformation test of disc 1*

Afterwards, for a better illustration of the strain hardening it was decided to deform disc 2 by about 8 mm. However, after a deformation of about 5 mm the surface of the recess crashed into the bolster plate. Thereby, the diameter of the supported ring was reduced and a higher force was needed for a further deformation of the disc. Furthermore, as the disc was not supported in the region of the T-slots of the bolster plate, it was distorted as shown in Figure 4.7.

Therefore, for the test on disc 3 a spacer ring was used as depicted in Figure 4.5. By this improvement it was possible to deform the disc by about 8 mm with a defined support at the outer edge of the disc recess.

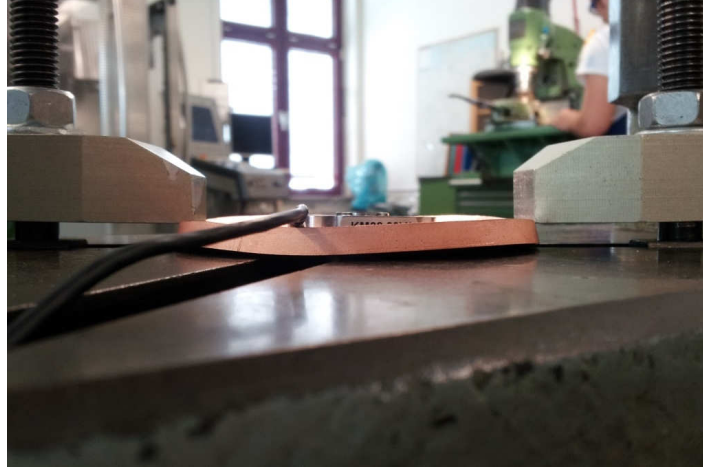


Figure 4.7.: *Distortion of disc 2 after collision with the bolster plate of the press*

4.2.4. Results

For the evaluation of the tests, first the signal from the force sensor had to be transferred into a force. Therefore, the output voltage V_{out} of the sensor was divided by the input voltage V_{in} to form the signal X of the sensor. In the test report of the sensor, values for the zero signal ($-0.00339 \text{ mV V}^{-1}$) and the signal at 20 kN (0.9991 mV V^{-1}) were given. In between these values the sensor had a linear behaviour. Thus the force F at a signal can be calculated by the linear function:

$$F = a \cdot X + b = a \cdot \frac{V_{out}}{V_{in}} + b \quad (4.1)$$

where a and b are calibration factors. As two points of the calibration curve are known, a and b can be calculated. Hence, Equation 4.1 follows to

$$F = 1.995 \cdot 10^7 \text{ N} \cdot \frac{V_{out}}{V_{in}} + 67.6 \text{ N}$$

and the force curve in Figure 4.8 can be plotted.

The data of force and deformation were collected by two different data acquisition units, which were not synchronised. However, for plotting a force-deformation diagram these data pairs need to be known for different time steps. Therefore, the force and the deformation curve were plotted in the same diagram, as shown in Figure 4.8. Then, by shifting one curve, the highest force was aligned with the maximum deformation. Additionally, the alignment of both curves was checked at times of significant force relief, where the deformation changed as well. This is indicated by the vertical lines in Figure 4.8.

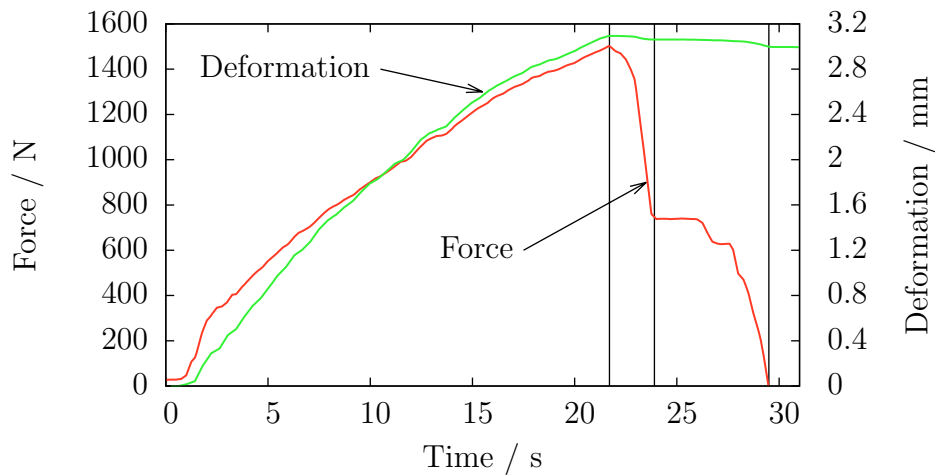


Figure 4.8.: *Alignment of force and deformation for the experiment on disc 1*

Furthermore, the time steps of the two data acquisition units were unequal. Therefore, a new time scale was built and for every time step the force and the deformation curves were interpolated. This guaranteed a data set of force and deformation at certain times. With the help of these data, the force-deformation curves in Figure 4.9 were plotted for each disc.

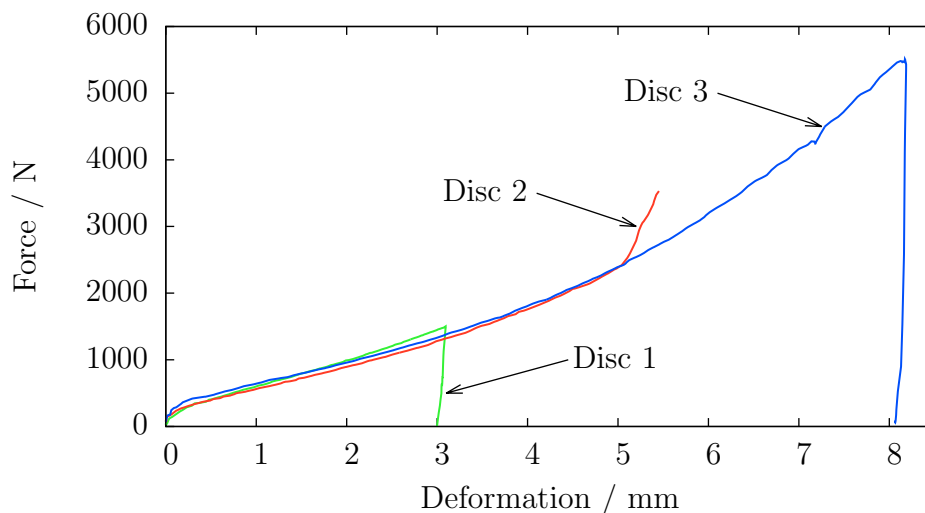


Figure 4.9.: *Force-deformation curves of the three test discs*

It can be observed that all discs showed a similar deformation behaviour. Already under a small load all discs deformed plastically. For a further increase of the applied force they deformed by nearly the same amount. The strong deviation of disc 2 at around 5 mm deformation is related to its collision with the bolster plate of the press. As this was not simulated later, the higher forces at disc 2 are not of interest and therefore are not depicted in Figure 4.9. However, before crashing into the bolster plate, disc 2 had the same deformation characteristic like disc 3.

4.3. Finite Element Analysis of Test Discs

After the experiments on the test discs were finished, the same problem was modelled in ANSYS Workbench. By the finite element analysis of the disc, the material model was further validated. This section describes the details of the FEA-model and the results of the validation.

4.3.1. Model Description

In the following all details for setting up the finite element analysis are described. This covers the designed geometry of the problem, the applied boundary conditions and the validation of the chosen mesh parameters.

Geometry

Since the discs were machined by turning and the load was applied symmetric to their centre axis, it was decided to model the problem as an axisymmetric 2D geometry. For this, within the Design Modeler of ANSYS Workbench, the half of the cross section of one disc was drawn in the first quadrant of the X-Y plane. In the sketch, the centre of the disc was aligned with the Y-axis, as shown in Figure 4.10. Here, all used dimensions are depicted. The thickness of 2.65 mm and 5.6 mm were parametrised according to Table 4.2.

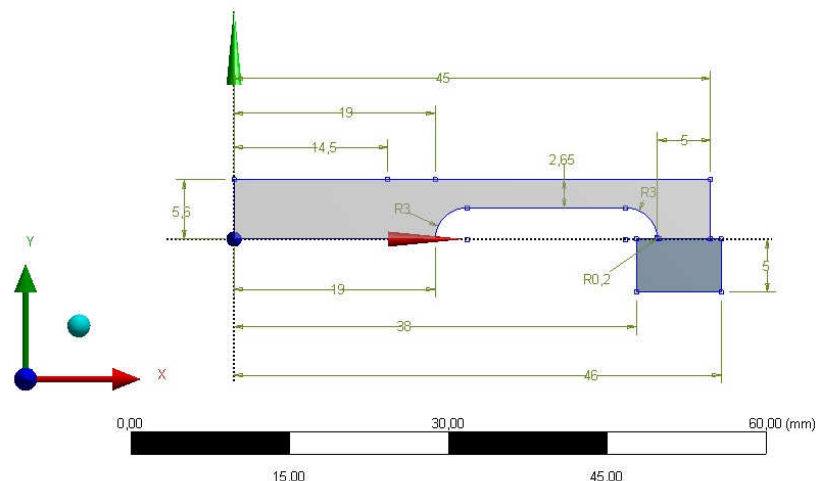


Figure 4.10.: *Designed axisymmetric 2D geometry for the finite element analysis, representing the test disc and the supporting spacer ring*

The top line - representing the top surface of the disc - was split into three sections

with the dimensions of the inner and outer diameter of the force sensor. Later, the load was applied to the middle section, to simulate the ring surface of the force sensor.

To enable a deformation of the supporting edge of the disc and to avoid a stress singularity in this point, a small round with a radius of 0.2mm was added to the edge¹. This is shown in Figure 4.11. Additionally, the problem was designed as a contact model to enable a sliding of the disc on its supporting surface. Therefore, an extra block, representing the spacer ring, was added to the sketch.

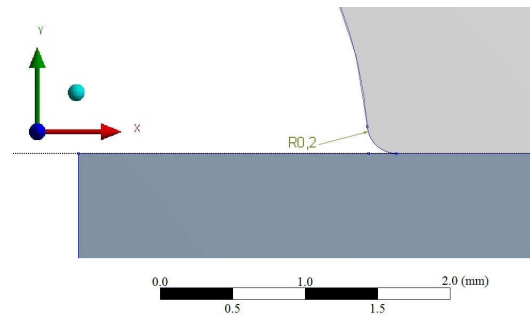


Figure 4.11.: Detail view of the supporting edge of the test disc

General Settings

In the Static Structural tool, the 2D behaviour of the geometry was set to axisymmetric. Afterwards, the material data of OFHC-Copper and stainless steel from Section 3.4 were assigned to the disc and the spacer ring respectively. Additionally, nonlinear effects for the material of the disc and large deflection in the solver controls were switched on.

Between the supporting edge of the disc and the top edge of the spacer ring a frictionless contact was arranged. This enabled a sliding of the disc on top of the spacer ring.

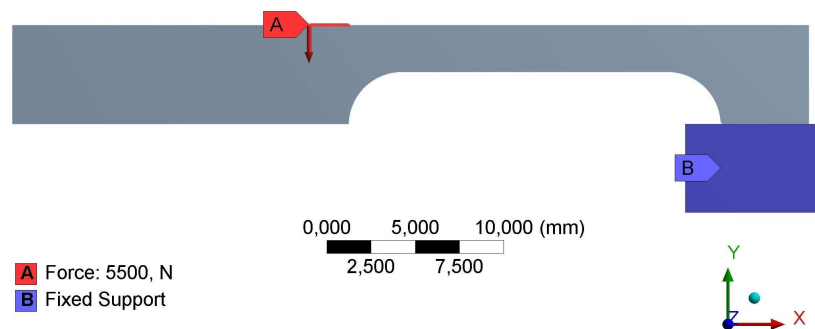


Figure 4.12.: Applied boundary conditions for the disc model

¹The dimension is reasonable due to a deburring of sharp edges after production.

On the middle section of the top edge of the disc, a load in form of a force was attached, as marked by A in Figure 4.12. It was altered in three load steps using 2000 N, 5500 N and 0 N. The load step of 2000 N was used to increase the number of result points in the transient region between elasticity and plasticity. The maximum load of 5500 N was chosen, as this was the highest force applied during the disc experiments. To obtain a detailed force-deformation curve, the first two load steps were split into 40 sub steps each, whereas the last load step was kept program controlled. The increased number of sub steps stabilised the force convergence of the solver additionally. Furthermore, the spacer ring was set as fixed support.

Mesh

For the problem the meshes shown in Figure 4.13 were used. Here, the spacer ring was meshed as one element only, because it should not undergo any deformation. Furthermore, the disc was meshed with an element size of 0.4 mm and a coarse relevance centre.

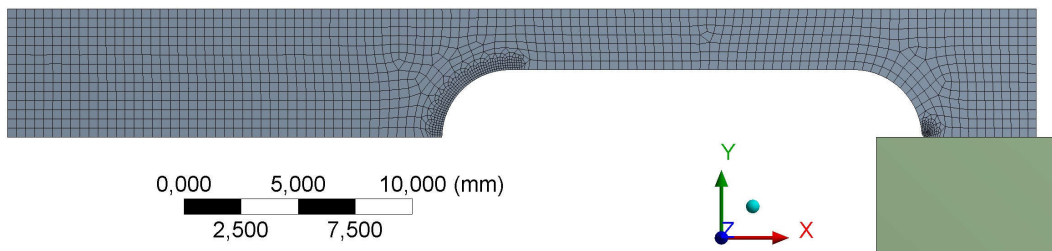


Figure 4.13.: Mesh used for the deformation simulations of the test disc

A three times finer mesh was chosen for the inner fillet of the recess and the supporting edge of the disc, shown in Figure 4.14. In these regions the highest stresses were assumed.

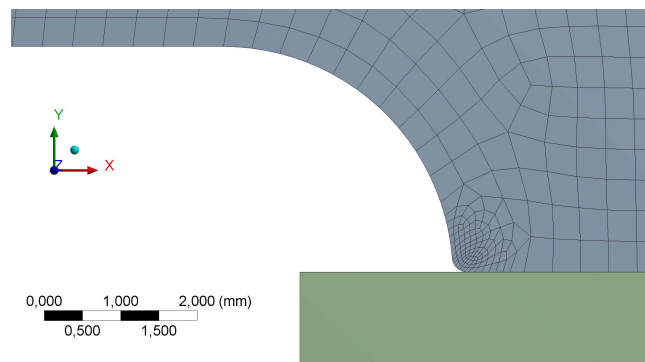


Figure 4.14.: Details of the refined mesh at the supporting edge of the disc

The mesh of the disc was formed by 1762 elements of the type PLANE183, which generated 5618 nodes. According to the ANSYS help [23], this type is a higher order 2D 8 node or 6 node element which exhibits quadratic displacement behaviour. Furthermore, it has plasticity, large deflection and large strain capabilities. Moreover, 27 elements of the type CONTA172 and TARGE169 were built in the contact region of the two parts. They represented a sliding between the surfaces of these parts.

In order to prove that the mesh is suitable for the investigated model, a convergence test was done to. Therefore, the mesh element size was reduced until there were only small changes (less than 1%) in the maximum stress and maximum deformation. The results are shown in Table 4.3 and Figure 4.15. As one can see, the deformation converged quite fast, whereas the stresses converged at an element size of 0.4 mm. In addition, the structural errors of the mesh elements were analysed. Here, the elements in critical areas did not show worse structural errors than the ones in the non-critical area. This further justifies the chosen mesh parameters.

Table 4.3.: *Convergence test of the mesh of the test disc*

Element size / mm	Number of nodes	Deformation max. / mm	Stress max. / MPa
1	1526	6.176	158.58
0.8	2117	6.180	161.74
0.5	3903	6.179	162.84
0.4	5618	6.179	163.34
0.3	8977	6.178	163.83
0.2	18259	6.176	164.44

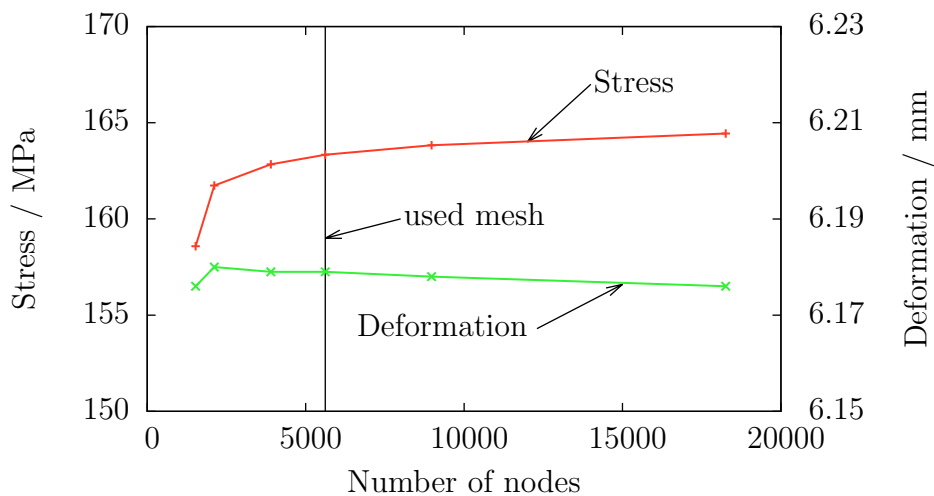


Figure 4.15.: *Convergence of stress and deformation at the test disc due to finer meshing*

4.3.2. Results

Figure 4.16 shows the simulated stress distribution under the load of 5500 N for the geometry of disc 1 and 3. As depicted, the strongest bending took place around the inner fillet of the recess. Therefore, the maximum stress of about 163 MPa occurred on the surface in this region. Furthermore, stresses above the yield strength of 35.5 MPa were calculated in nearly all domains of the disc. This indicated that the whole disc exhibited plastic deformation.

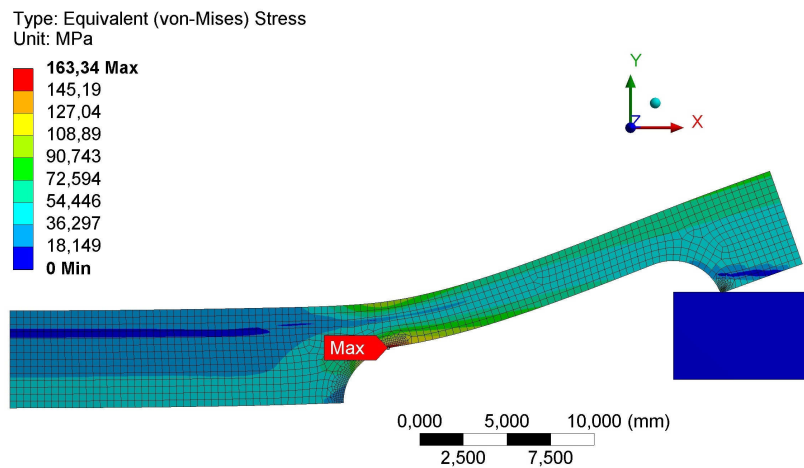


Figure 4.16.: *Stress distribution at the test disc under a load of 5500 N, deformation depicted in true scale*

In Figure 4.17 the supporting edge of the disc is depicted. The edge transmitted the applied load from the press ram to the spacer ring. Due to the small contact surface, the stress in the edge became fairly high which resulted in a small deformation of it.

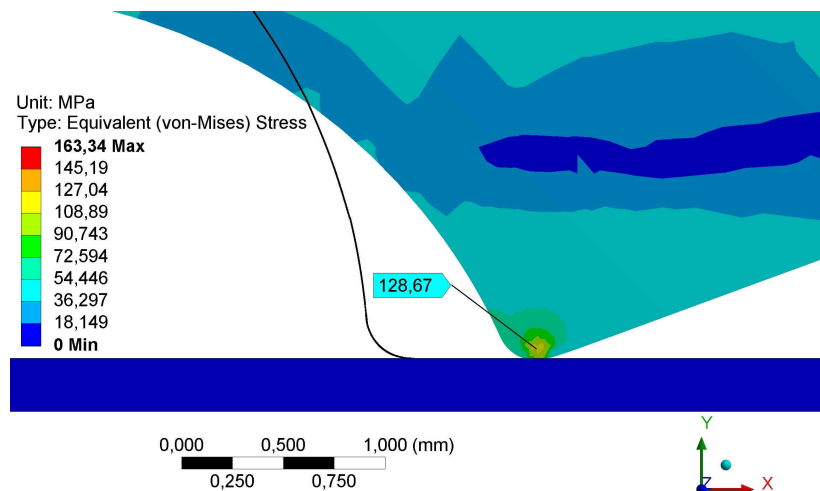


Figure 4.17.: *Detail view of the stress distribution at the supporting edge of the test disc, shown in the deformed state and with the wire frame of the undeformed geometry*

By comparing the deformed shape of the disc with the wire frame of the undeformed geometry, one can see, that the supporting edge moved outwards. This validates the chosen contact condition and shows an expected deformation behaviour of the disc.

Additionally, the influence of the geometry was analysed. Therefore, the force-deformation curves of the two different geometries of the test discs are plotted in Figure 4.18. As expected, for the thinner disc 2 a higher deformation than for disc 1 and 3 was simulated. Moreover, the force-deformation curves illustrate the plastic behaviour of the material model. They show a nonlinear characteristic with a remaining plastic deformation after unloading.

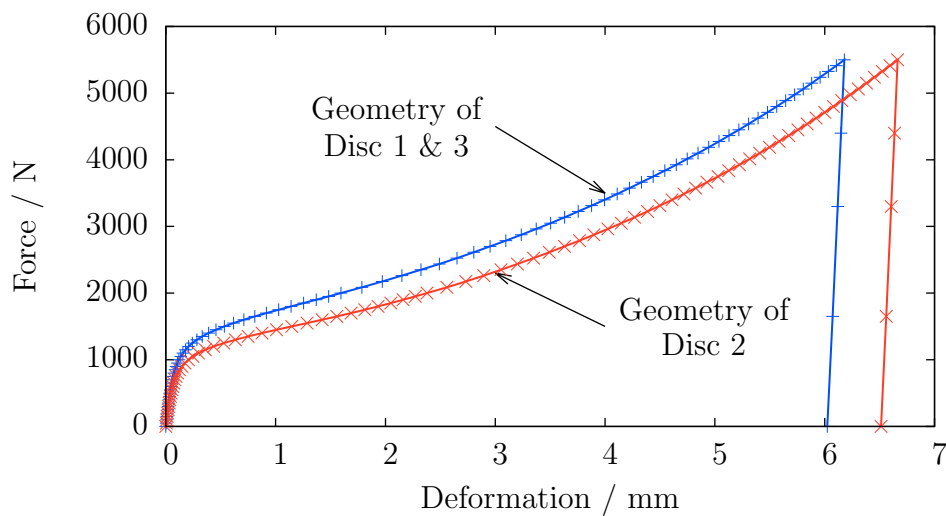


Figure 4.18.: Influence of the geometry of the test discs on the deformation behaviour

As the Poisson's ratio was not measured during the material tests, deformation analyses with changed Poisson's ratio were done. The results of the simulations are shown in Table 4.4. Here, one can see that the Poisson's ratio influenced the deformation result by some micrometers only. As this can be neglected, the previous chosen value of 0.34 was used for further analyses.

Table 4.4.: Influence of the Poisson's ratio

Poisson's ratio	0.2	0.34	0.45
Maximum deformation / mm	6.185	6.179	6.173
Plastic deformation / mm	6.026	6.024	6.024

4.4. Discussion

After the measurements and simulations were finished, the results were compared. This is shown in Section 4.4.1. As the outcome showed some deviations, an error analysis was performed.

4.4.1. Comparison of Simulations and Experiments

As a first indication whether the material model worked, the results of the simulations of the tensile test were compared with the measurements. Afterwards, this was done for the test discs, respectively.

Tensile Test

In Figure 4.19 the measured forces and elongations from the tensile test of specimen 4 are plotted. Additionally, in the same diagram the simulated directional deformation of the tensile beam at certain forces is plotted as points. As one can see, the results of the finite element analysis are in good agreement with the measurement. Thus, the material model works for the tensile beam and the correct dimensions for the material data were used. However, as during the tensile test the specimens were not unloaded, the comparison only proves the nonlinear deformation behaviour of the material, but does not show any permanent deformation.

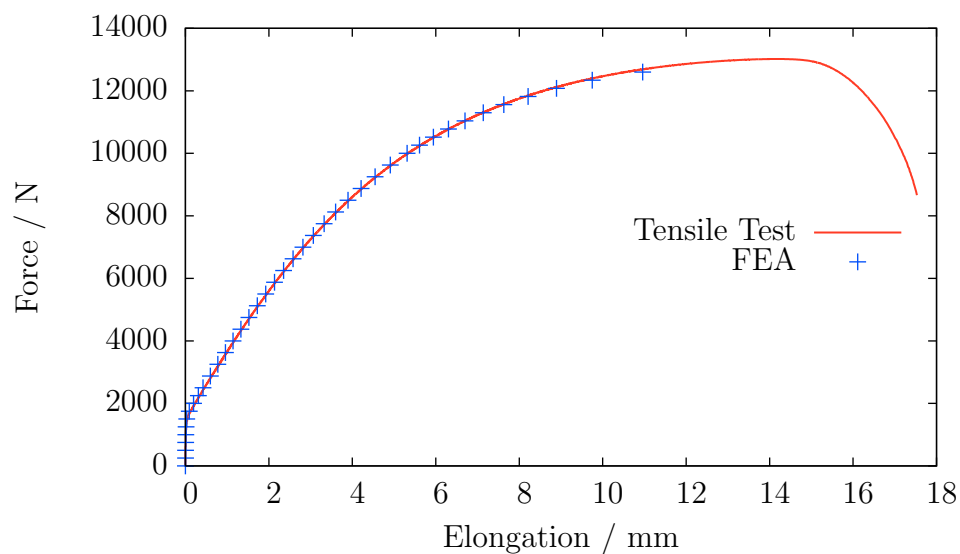


Figure 4.19.: Comparison of the tensile test measurements for specimen 4 with the simulation results

Test Discs

Figure 4.20 shows a comparison of the measured and simulated force-deformation curves for the different test discs. Here, one can see that the discs in the experiments behaved softer than simulated by the finite element analyses. Under the same load they showed larger deformations than in the simulations. Thus, the material model did not match the real material behaviour.

However, in the simulations the change in the geometry had an influence on the deformation of the discs. This was not the case in the experiments. As an influence of the geometry is reasonable, it suggests that there were some irregularities during the measurements on the discs.

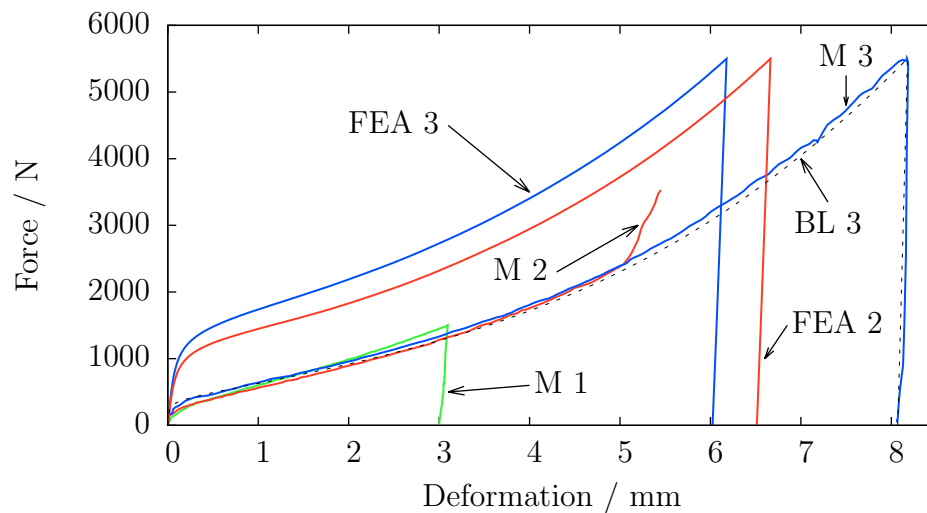


Figure 4.20.: Comparison of the test disc measurements with the results of the simulations; the measurements of disc 1 to 3 are labelled with M 1 to 3; FEA 2 and 3 correspond to the simulations for the geometry of disc 2 and 3; and BL 3 represents a bilinear material model applied on disc geometry 3

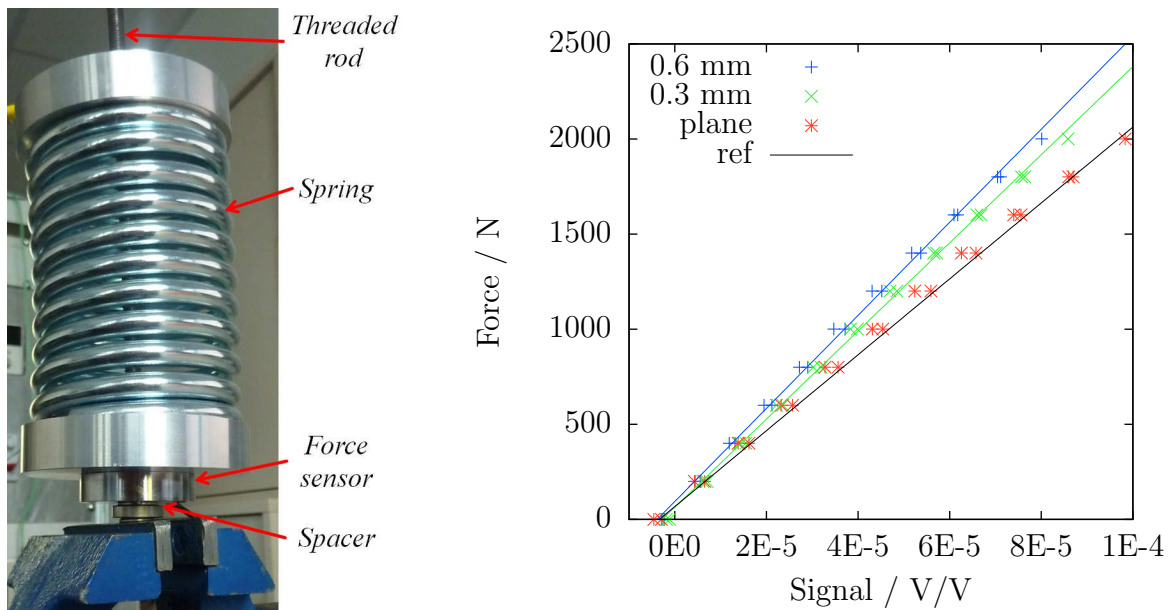
To simulate the deformation behaviour of test disc 3, a new material was built in the Engineering Data of ANSYS Workbench. To have only a limited number of parameters to form the new stress-strain curve, bilinear isotropic hardening was chosen to simulate the plasticity of the material. For the material, the Young's modulus was defined to be 90 GPa and the Poisson's ratio was set to 0.34. Afterwards, the yield strength and the tangent modulus of the bilinear isotropic hardening model were changed. This was done until the simulated force-deformation curve matched the one measured for test disc 3. In Figure 4.20 the final force-deformation curve by the bilinear material simulation is labelled with BL 3 and depicted in dashes. It represents the deformation behaviour of disc 3 quite well. For bilinear material model a yield strength of 6 MPa and a tangent modulus of 1450 MPa was used.

4.4.2. Influences on the Measurements

As the simulation of the tensile beam showed a good agreement with the its measurements, the material model of multilinear isotropic hardening was assumed to be correct. Therefore, the deviations between the simulations and the experiments were suspected to be due to experimental errors during the measurements on the test discs. Calibration tests were done to verify the accuracy of the sensors, that were used for the disc experiments.

First, the length gauge was checked by measuring several gauge blocks. The gauge blocks had an accuracy of ± 0.005 mm. By placing the gauge blocks between the length gauge and a fixed plate the reading always corresponded to the nominal length of the gauge block. This proved that the accuracy of the length gauge was by far sufficient.

Afterwards, the calibration of the force sensor was checked. Therefore, a spring with known spring rate was used to apply a defined force on the force sensor. Figure 4.21(a) shows the experimental set-up for the calibration of the force sensor at which the spring was compressed via tightening a nut on the threaded rod. As the threaded rod was plugged through the force sensor the full load of the spring was applied to the sensor.



(a) Experimental set-up for the calibration of the force sensor

(b) Different calibration curves for the force sensor under plane and inclined applied forces; inclination caused by spacers with various thickness

Figure 4.21.: Calibration of the force sensor

By compressing the spring, different forces were adjusted and the signals of the sensor for each force step were taken. In Figure 4.21(b) the data sets of force and signal are plotted. Here one can see that for a perpendicular applied force - by a plane surface -

the reference calibration curve of the supplier is applicable.

However, the influence of a tilted surface was tested as well. Therefore, spacers with a thickness of 0.3 mm and 0.6 mm were placed eccentric between the nut on the threaded rod and the smaller supporting surface of the force sensor. As shown in Figure 4.21(b) the calibration curves for an inclined applied force differ from the reference curve. For instance an inclined applied force of 2000 N for the 0.6 mm spacer would result in a measured value of 1600 N. As the parallelism between the press ram and the bolster plate could not be determined, the sensitivity of the sensor to inclined loads might had an influence on the measurements. However, this influence was not as strong to cause the large deviations between the simulations and the experiments.

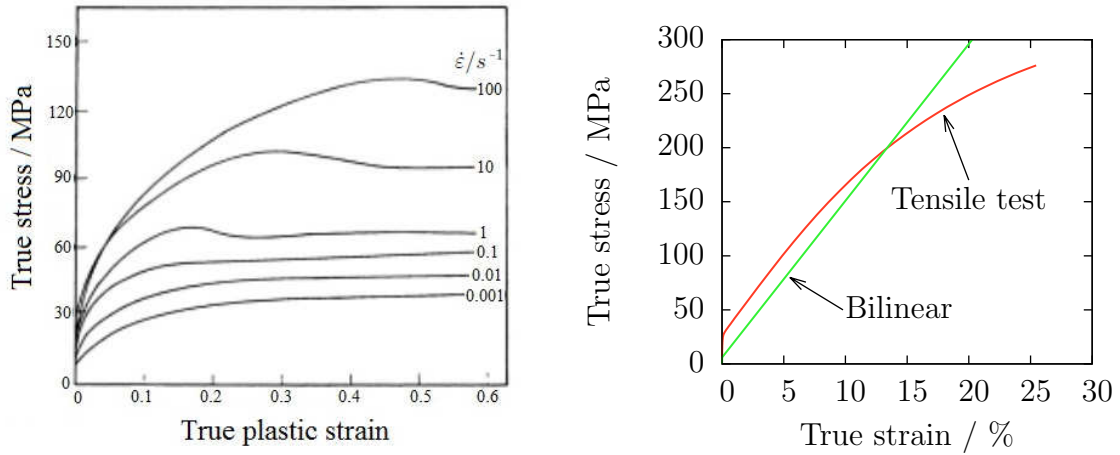
Furthermore, during the tensile tests and the deformation tests of the discs different strain rates were used. The strain rate indicates how fast a material is deformed and is defined by the change of strain with respect to time. The tensile tests were performed with a constant stress rate of 10 MPas^{-1} . Due to the effect of strain hardening this resulted in a non-constant strain rate. However, for an estimation of the average strain rate in Figure 3.5 the stresses at a strain of 30% were about 200 MPa. With the given stress rate this results in a strain rate of about 0.015 s^{-1} for the tensile test.

In contrast, the experiments on the test discs were performed with much smaller strain rates to obtain as many data sets as possible. Furthermore, due to the more complex shape of the discs, the straining differed over the cross section of the discs. Therefore, different strain rates were expected for the different regions. However, to give an estimation for the maximum strain rate, from the simulations of the deformation of disc 3, a maximum strain of about 10% was read. Additionally, the maximum deformation was applied within 30 s. From this it follows that the maximum strain rate for disc 3 was about 0.0033 s^{-1} . This value was similar for the other discs. Thus the strain rate during the tensile test was in minimum five times higher than for the experiments of the test discs.

To show the influence of the strain rate on the stress-strain curves, in Figure 4.22(a) three true stress-strain curves for OFHC-Copper at different strain rates are depicted. These data were taken at a temperature of 700°C [28]. They indicate a remarkable influence of the strain rate.

For a comparison between the tensile test and the disc experiments, in Figure 4.22(b) the true stress-strain curve obtained by the tensile test and the bilinear true stress-strain curve adjusted to the disc experiments are plotted. In the strain range below 10% the bilinear curve is offset to the true stress strain curve of the tensile test. This offset is most properly due to the different strain rates. Therefore, the differences

in the strain rate is the most reasonable justification for the deviations between the measurements and the simulations.



(a) True stress-strain curves for OFHC-Copper at 700°C for various strain rates; from [28]

(b) True stress-strain curves obtained by the tensile test and by adjusting the simulations to the disc experiments

Figure 4.22.: Influence of the strain rate on the true stress-strain curve of OFHC-Copper

4.4.3. Conclusions

In this chapter the simulation of the tensile beam was shown. The result of the deformation analyses were in good agreement with the measurement data from the test. This validates the chosen material model to be applicable for the simulations.

Furthermore, deformation experiments on test discs were performed, which were simulated as well. Here, the comparison of the deformation during the experiments with the simulated deformation showed, that the real discs behaved softer than simulated. This difference is probably caused by the use of different strain rates during the tensile test and the deformation of the discs, which could not be fully clarified in the scope of this thesis. Additionally, the deformation tests showed how important validation experiments are.

These result suggest that the material model obtained by the tensile test should be used for the review of the tuning device. It assumes the material to be harder than during the experiments on the test discs. Thereby, higher forces might be simulated for the deformation of the gun, resulting in a stronger gear system to be chosen. Thus, even if the real material behaves softer during the tuning procedure, the gear system will be capable of all tuning demands.

5. Finite Element Analysis of the Proposed Gun

Using the material model obtained in Chapter 3 it was possible to simulate the mechanical tuning of the planned Gun 5. This cavity will consist of three OFHC-Copper parts which together form the two gun cells. For the tuning of the $\lambda/2$ cell the load of the tuning device will be applied to the front end of the gun and for the $\lambda/4$ cell to the back plane. Figure 5.1 shows the positions where the thrust bush will be applied for the tuning of each cell.

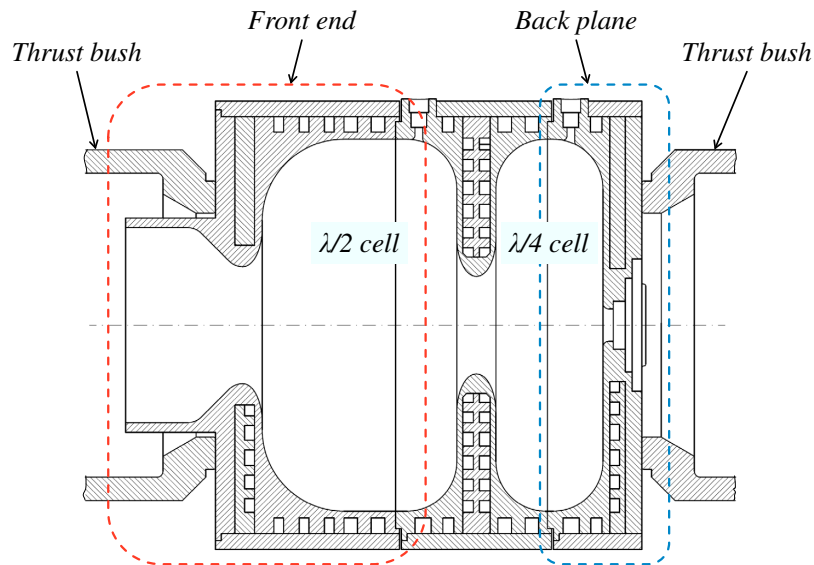


Figure 5.1.: Gun cavity type 5

As the tuning processes of both cells are independent from each other, it was decided to perform the simulation by two simplified models: one representing the front end and a second representing the back plane of the gun. This chapter gives a detailed description of the models and depicts the forces required for the tuning of the gun.

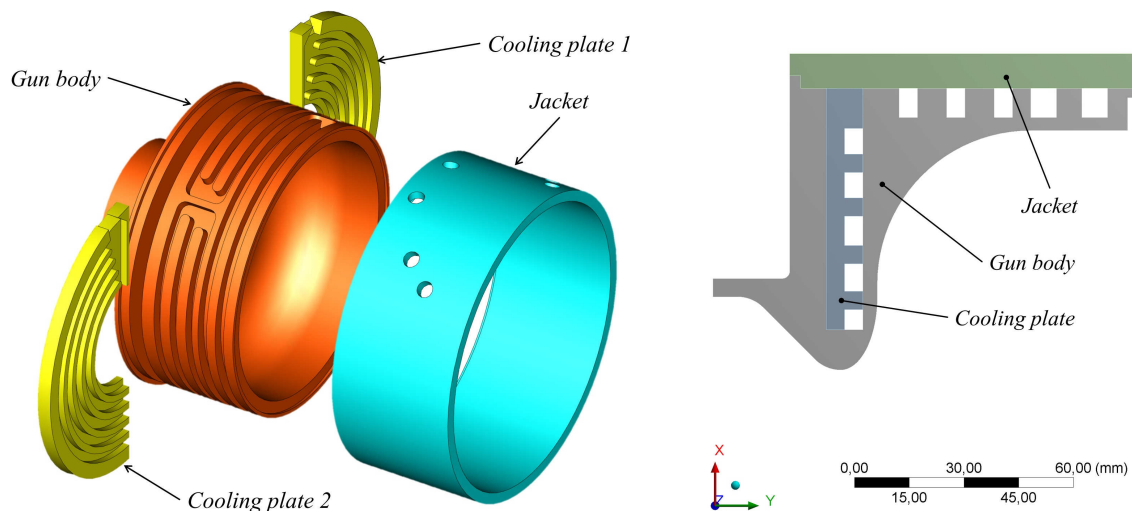
5.1. Analysis of the Front End

In this section the model of the front end of the gun is described. The first part shows the simplifications of the geometry, the applied boundary conditions and the chosen mesh parameters. In the second part the results of the deformation analysis are depicted and the influence of a reduced wall thickness is discussed.

5.1.1. Model Description

The front end of the gun is designed with four parts as shown in Figure 5.2(a). Here, the two cooling plates will be inserted in the groove of the gun body. Afterwards, the jacket will be slipped over the gun body and all parts are brazed together. Thereby, channels are formed through which cooling water is pumped during operation. For the gun body and the cooling plates OFHC-Copper is foreseen. To protect these soft parts the jacket will be made from stainless steel.

As the parts are axisymmetric - except for some details which were neglected for the deformation analysis - the half of their cross sections were designed in the Design Modeler of ANSYS Workbench to build the 2D model shown in Figure 5.2(b). In the model the Y-axis was used as centre axis as required for 2D axisymmetric analyses.



(a) 3D model of the front end of Gun 5; design by V. Paramonov

(b) Simplified 2D model used for the finite element analysis

Figure 5.2.: Simplification on the front end geometry in order to use a 2D model for the finite element analysis

In the Static Structural tool the corresponding materials were assigned to the geometries. For the parts made of OFHC-Copper the material model obtained by the tensile

tests depicted in Section 3 was used. Additionally, nonlinear material effects were switched on and the 2D behaviour of the geometry was set to axisymmetric. In the solver controls large deflection was activated and weak springs were suppressed.

Furthermore, the connections between all parts were modelled as bonded contacts. As these connections will be brazed this type of contact is valid. However, the real connections might be weaker if the solder does not wet the whole surface. As these brazing processes are difficult to predict idealised conditions were assumed. Additionally, the perfect bonded connections stiffens the geometry which results in higher loads for its deformation. For the review of the tuning device this gives an additional safety factor.

Figure 5.3 depicts the applied boundary conditions. The model was tested with different forces to deform the structure. For this all forces were applied to a ring surface with the dimensions of the thrust bush.

As the analysed gun body will be brazed to the next gun body to form the $\lambda/2$ cell, fixed supports were applied on their contact surfaces. This was assumed to be reasonable as the majority of the force will act perpendicular to the front face of the subsequent gun body.

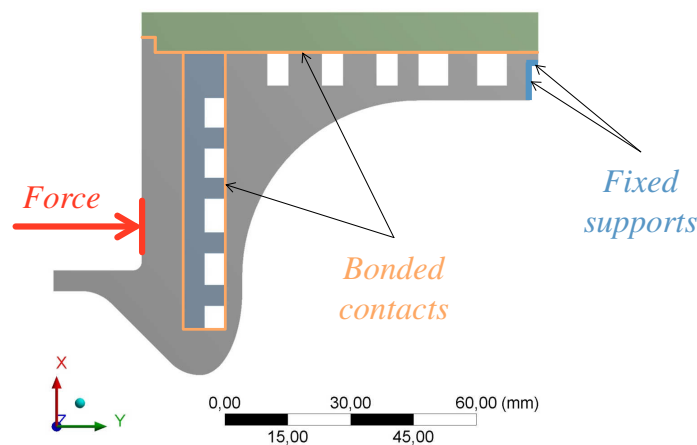


Figure 5.3.: Location of the applied boundary conditions and the contact surfaces

The mesh used for the analysis is shown in Figure C.1 in Appendix C. All parts were meshed with an element size of 1 mm and a medium relevance centre. Additionally, in the labelled regions the mesh was refined as depicted. In the refined regions high stresses were assumed. Thereby, 5647 elements of the type PLANE183 with 18258 nodes were built, whose behaviour is described in Section 4.3.1. Additionally, in the contact regions 594 elements of the type CONTA172 and TARGE169 were formed. They enabled the bonded contacts at which the parts did not penetrate each other.

For validating the chosen mesh parameters the stresses for a reduced element size

of 0.4 mm were compared to those at an element size of 1 mm. Due to the sharp edges of the gun body stress singularities occurred on the jacket in the contact region between both parts. These locations are highlighted in Figure 5.4. Here, the stresses increased for the refined mesh. The singularities are based on the assumption of a perfectly bonded connection where the parts can not move with respect to each other. However, in reality the solder will allow small movements which will reduce the stresses dramatically. Therefore, the stress singularities were neglected for the given problem.

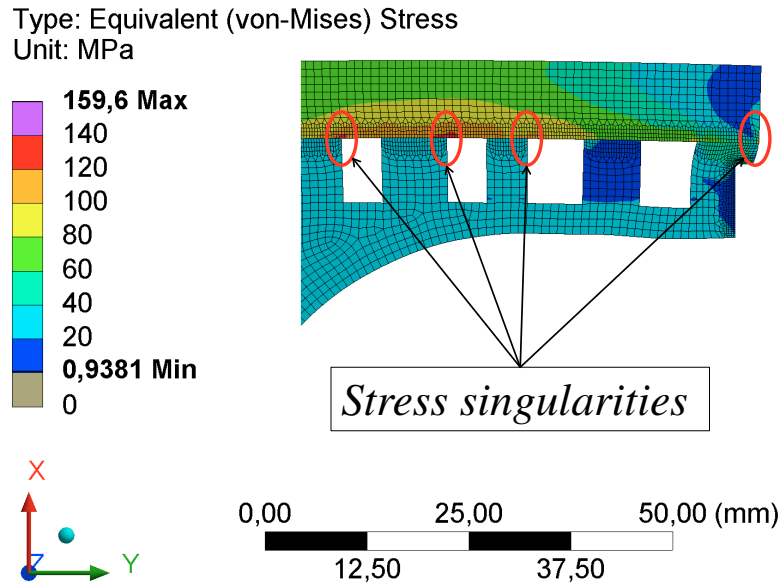


Figure 5.4.: Locations of stress singularities in the contact region between the gun body and the jacket under a load of 200 kN and with an element size of 1 mm

For the rest of the geometry the stresses did not change with reduced element size. To illustrate this Figure C.2 shows the stress distribution calculated with an element size of 1 mm and Figure C.3 depicts the one for an element size of 0.4 mm. Both figures are plotted with the same colour bands. Since the stress distribution did not change for the refinements, the mesh with the element size of 1 mm was used for further analyses.

5.1.2. Results

A force of 200 kN was simulated on the front surface of the gun body, to obtain a sufficient plastic deformation. Under this load the structure showed a maximum deformation in Y-direction of 0.49 mm. The deformed shape is shown in Figure C.4. In a second load step the force was set to zero and the model exhibited a remaining plastic deformation in Y-direction of 0.38 mm. By this deformation analysis the force-deformation curve in Figure 5.5 is plotted.

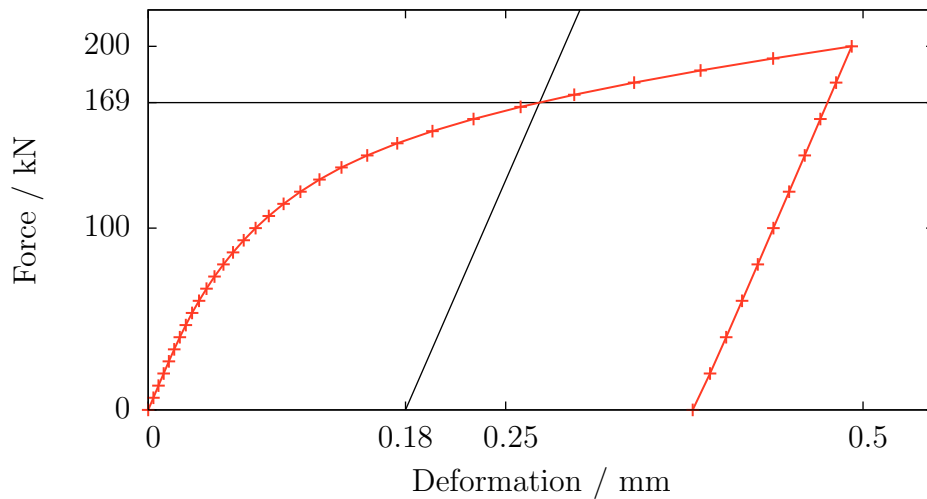


Figure 5.5.: Force-deformation curve for the tuning of the front end of Gun 5; constructed lines indicate a plastic deformation of 0.18 mm which corresponds to a tuning of the gun by 2 MHz

As described in Section 2.1.2 for the latest tuning of a Gun 4 a frequency shift of 2 MHz had to be compensated. For this a plastic deformation of the $\lambda/2$ cell by 0.18 mm was demanded. To estimate a compensation of the same frequency shift on Gun 5, in Figure 5.5 an additional line parallel to the end section of the force-deformation curve was constructed. It intersects the deformation axis at 0.18 mm. From its intersection with the force-deformation curve it can be observed that a force of 169 kN is needed in order to plastically deform the front end of Gun 5 by 0.18 mm.

However, as the design of Gun 5 is not finished, analyses with reduced thickness of the front wall were performed. For this the dimensions of the recess of the gun body and its front wall were changed as shown in Figure 5.6.

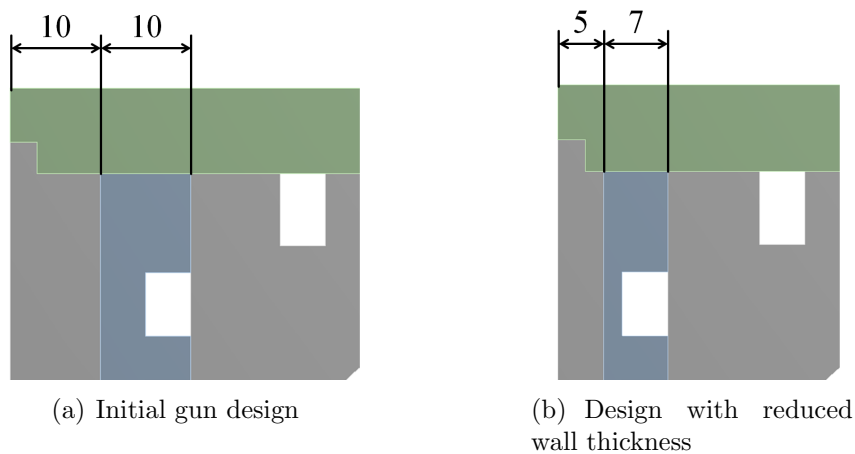


Figure 5.6.: Reduction of the wall thickness of the front end of the gun in order to lower the deformation forces

This resulted in lower forces to be calculated for the tuning of the gun. Figure C.5 shows the deformed shape of the front end under a load of 140 kN. Here, the vertical section of the inner surface is shifted in parallel and the maximum deformation occurs around the centre of that section.

Furthermore, the force-deformation curve depicted in Figure 5.7 was obtained. It can be seen that a force of 116 kN is required to tune the gun by 2 MHz.

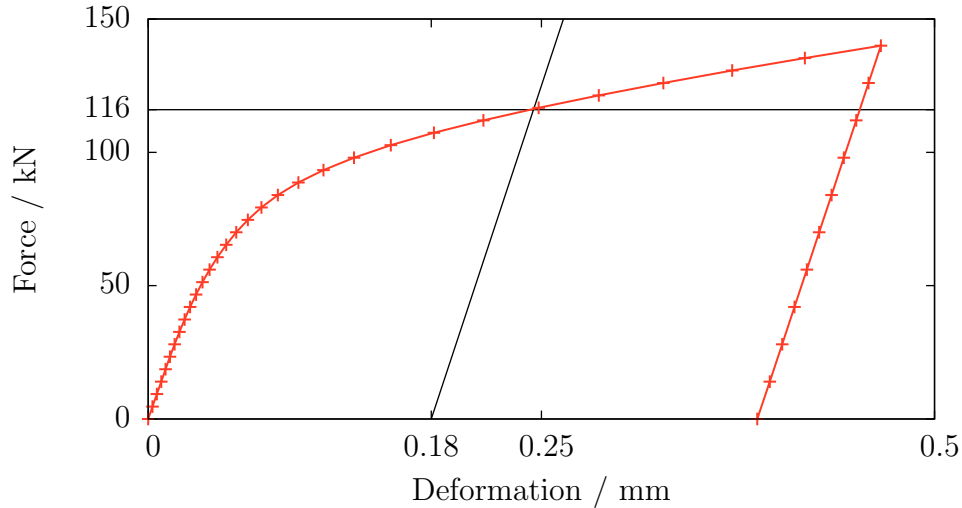


Figure 5.7.: Force-deformation curve for the tuning of the front end with reduced wall thickness; constructed lines indicate a plastic deformation of 0.18 mm which corresponds to a tuning of the gun by 2 MHz

5.2. Analysis of the Back Plane

This section describes the deformation analysis of the back plane of the gun. This side has no influence on the resonance frequency of the cavity but its deformation is important for adjusting the position of the photo cathode with respect to the electric field maximum in the $\lambda/4$ cell.

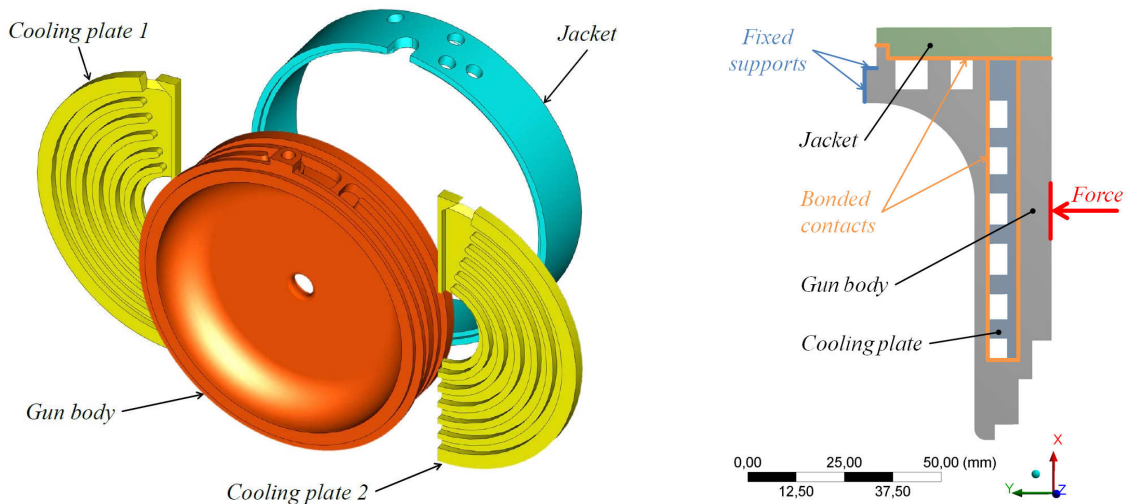
5.2.1. Model description

The back plane has a similar design like the front end of the gun. It also consist of four parts as shown in Figure 5.8(a) and is assembled as described in Section 5.1.1. Furthermore, all parts are made of the same material as the parts of the front end.

To build a 2D model of the back plane details were neglected again. In the Design Modeler of ANSYS Workbench the geometry was designed as axisymmetric model,

5. Finite Element Analysis of the Proposed Gun

using a sketch of one half of its cross section. This is shown in Figure 5.8(b). However, as the design is still in progress the dimensions of the recesses on the right might change. Also, a tube will be brazed in one recess, which will stiffen the back plane. Therefore, detailed analyses have to be performed on the final design. Nevertheless, the results of the depicted analysis serve as an approximation of the deformability of the back plane.



(a) 3D model of the back plane of Gun 5; design by V. Paramonov

(b) Simplified 2D model used for the finite element analysis

Figure 5.8.: *Simplification on the back plane geometry in order to use a 2D model for the finite element analysis*

The same material properties and solver settings as for the front end were chosen in the Static Structural tool. Between all parts bonded connections were assumed. The locations of the applied force, the bonded contacts and the fixed support are shown in Figure 5.8(b).

As the mesh was validated for the front end model and the design of the back plane is similar, the same element size of 1 mm was chosen. Furthermore, a finer mesh was used in areas of high stresses as shown in Figure C.6.

5.2.2. Results

To obtain a plastic deformation of more than 0.2 mm a force of 110 kN was simulated on the back plane model. The resulting stress distribution is shown in Figure C.7. Here again stress singularities occurred at the bonded connection between the gun body and the jacket. As described in Section 5.1.1 these singularities can be neglected because they are based on the assumption of a perfect bonded connection, which will not exist in reality.

The directional deformation under the load is shown in Figure C.8. Here the inner ring, where the cathode will be located, is deformed most. This is favoured as the position of the cathode should be adjusted by the tuning of the back plane. Additionally, from the analysis of the directional deformation the force-deformation curve in Figure 5.9 was obtained. In it the required force for a tuning of 0.2 mm is constructed exemplary. It was found to be 98 kN.

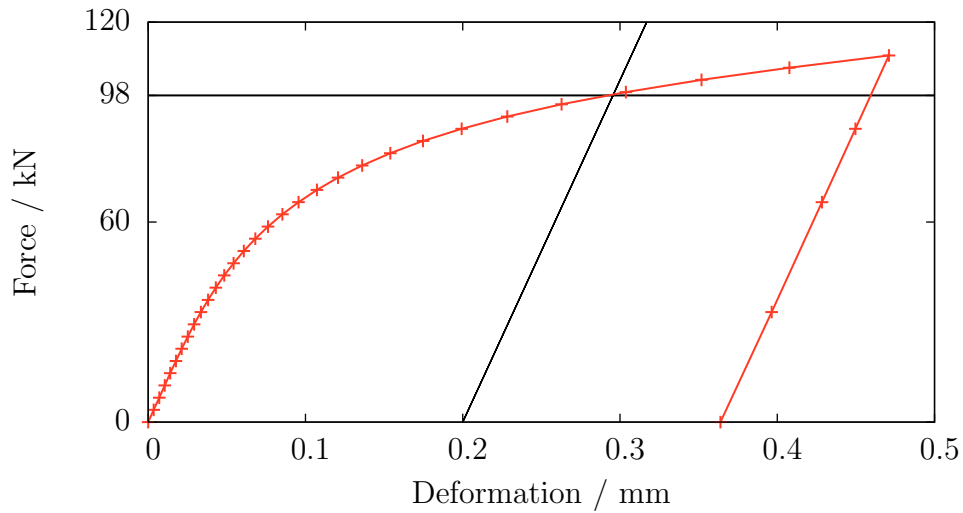


Figure 5.9.: Force-deformation curve for the tuning of the back plane; constructed lines indicate a plastic deformation of 0.2 mm

This shows that a lower force is required for the tuning of the back plane as for the front end of Gun 5. Therefore, for the review of the tuning device the analyses of the front end are more significant.

6. Conclusions and Outlook

The material tests described in Chapter 3 showed that the annealed OFHC-Copper had a tensile ultimate strength of 220 MPa, a yield strength at 0.2 % strain offset of 30 MPa and a Young's modulus of 90 GPa. These values are reasonable for soft copper and in good agreement with the stress-strain curve presented in [17]. Furthermore, the tests were performed on two test dates and the OFHC-Copper did not show any hardening over seven weeks. The averaged stress-strain data can be found in Appendix B.

A finite element analysis of the tensile test showed that the plasticity model was sufficient accurate, as the simulated and the measured force-deformation curves displayed a good correlation. However, by deformation experiments on test discs less correlation was found between measurements and simulated results. During the experiments the discs behaved softer than simulated. This is possible due to a lower strain rate used for the disc experiments than for the tensile tests. In the scope of this thesis the differences between the disc simulations and the measurements could not be fully analysed.

Although it turned out that the real material behaves softer, the material model obtained by the tensile test was used for the design analyses of Gun 5. This results in an additional safety factor for the review of the tuning device.

The deformation analyses were performed separately for the front end and the back plane of the gun. As shown in Chapter 5, for the deformation of the back plane a lower force was required than for the front end. Thus, if the tuning device is capable to deform the front end of the gun, the back plane can be also tuned.

The simulations for the front end of the gun showed that for compensating a frequency shift of 2 MHz a force of 169 kN is required as shown in Figure 6.1. This force is much higher than the force of 25 kN which can be applied by the current tuning device. The simulations further showed that with the current spindle gear of the tuning device the gun can be deformed elastically only.

To lower the required tuning force, additional analyses with a reduced thickness of the front wall of the gun were performed. Such changes might be considered as the design of Gun 5 is still in progress. As shown in Figure 6.1 the reduction of the wall thickness

had a remarkable influence on the deformation behaviour of the gun and lowered the tuning force to 116 kN. However, this force is still much higher than the 25 kN which can be applied by the current tuning device.

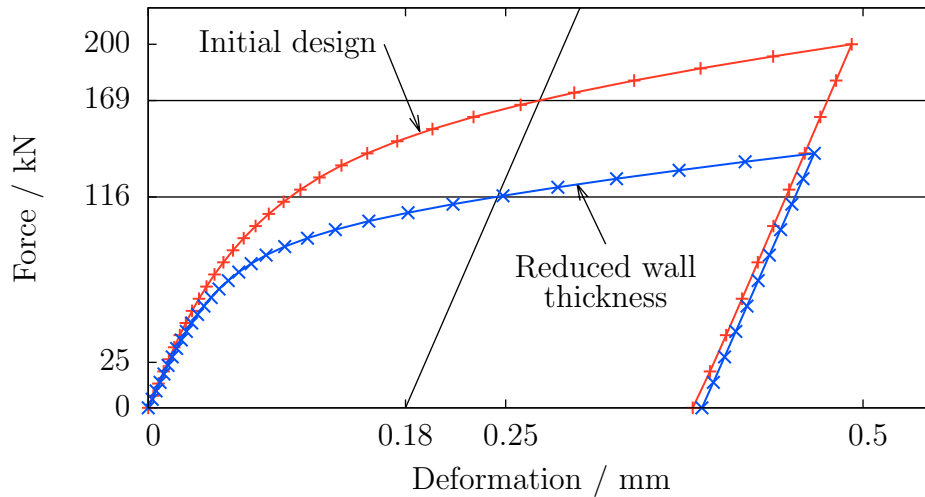


Figure 6.1.: Force-deformation curves for the tuning of the front end of Gun 5; constructed lines indicate the plastic deformation of 0.18 mm which corresponds to a tuning of the gun by 2 MHz

This work showed that in order to be able to tune Gun 5 the tuning device needs to be equipped with a stronger spindle gear. For the current design of Gun 5 it should have at least a capability of 200 kN. By the use of such a high load the entire rig of the tuning device might be reviewed.

Additionally, during the ongoing design process of Gun 5 its deformability should be considered. Therefore, the geometry might be changed further. This work provides the necessary tools for analyses of changed geometries.

To clarify the influence of the strain rate during the deformation of OFHC-Copper further test are required. Such tests will increase the accuracy of the analyses of plastic deformation.

A. Technical Data Sheets

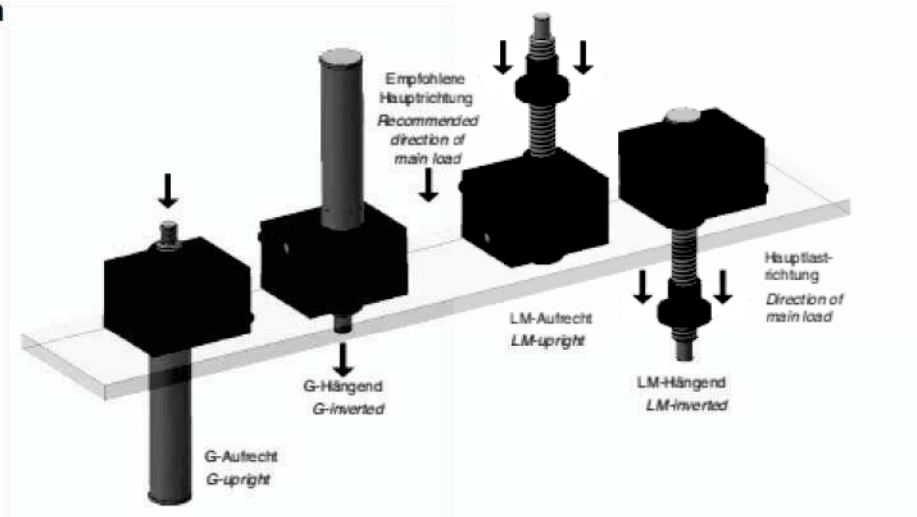
List of technical data sheets attached:

- Spindle gear SHG-MJ3-L by [10]
- Flexible coupling type 300-40 by [9]

TYPENÜBERSICHT

HUBGETRIEBE

Aufbauarten



mit Trapezgewindespindel

Baugröße/Typ	MJ0	MJ1	MJ2	MJ3	MJ4	MJ5	BJ1	BJ2	BJ3	BJ4	BJ5
Belastung kN max. statisch	2,5	5	10	25	50	100	150	200	250	350	500
Spindel TR	16x4	18x4	20x4	30x6	40x7	55x9	60x9	70x10	80x10	100x10	120x14
Übersetz.verhältnis N	4:1	4:1	4:1	6:1	7:1	9:1	9:1	10:1	10:1	10:1	14:1
	L 20:1	16:1	16:1	24:1	28:1	36:1	36:1	40:1	40:1	40:1	56:1
Leerlaufdrehm. Nm N	0,03	0,05	0,12	0,17	0,24	0,82	0,9	1,3	1,42	1,65	1,97
	L 0,02	0,04	0,09	0,12	0,26	0,5	0,58	0,98	1,09	1,15	1,4
Wirk.grad theor.% N	38	31	30	29	26	22	20	19	18	17	16
	L 30	28	27	26	23	20	18	17	16	15	14
Hub/Umdrehung N	1					1					
	L 0,2					0,25					
Drehmoment bei N	1,5	3,2	7	16	34	69	105	150	205	300	425
	L 0,7	1,4	2,5	5,2	10,2	30	28	60	92	120	150
Gewicht ohne Hub in kg	0,6	1,2	2,1	6	17	32	41	57	57	85	100
Gewicht in kg pro 100 mm Hub	0,1	0,25	0,45	0,7	1,2	2	2,4	2,2	4,2	6,6	10,3

mit Kugelgewindespindel

Baugröße	MJ1-KGT	MJ2-KGT	MJ3-KGT	MJ4-KGT	MJ5-KGT
Belastung kN (dyn.)	5	8	9,5/26	19/30	55
Spindel KGT (gerollt)	1605	2005	2505/3210	4005/4010	5010
Übersetzverhältnis N	4:1	4:1	6:1	7:1	9:1
	L 16:1	16:1	24:1	28:1	36:1
Leerlaufdrehmom. Nm	0,03	0,07	0,1	0,25/0,22	0,5
Wirkungsgr. %	60	59	57	55/57	55
Hub/Umdrehung N	1,25	1,25	0,83/1,66	0,71/1,43	1,11
	L 0,31	0,31	0,21/0,63	1,18/0,36	0,28

Flexible Schalenkupplung TYP 300 - bis 200 Nm

Eigenschaften:

- Einbau ohne Verschieben der Wellen
- Einsatz auch bei sehr hohen Drehzahlen
- Spielfrei
- Einsatztemperatur bis 200°C
- Einschnitte mit Vollradius
- Alu-Legierung

Anwendung:

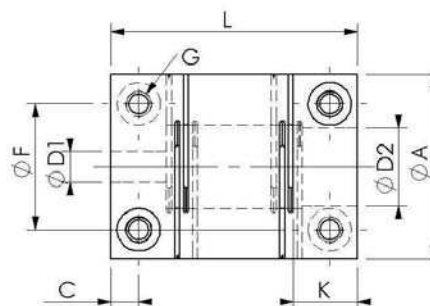
- Industrieroboter
- Handhabungsgeräte
- Verpackungsmaschinen
- Textilmaschinen
- Holzbearbeitungsmaschinen

Bei den Größen 20, 30 und 40 liegt die Anwendung z. B.:

Anbau von

- Inkrementalgeber
- Schrittmotore
- Tachogeneratoren u. s. w.

TYP 300 - bis 200 Nm



Größe	M_N (Nm)	Zul. Wellerversatz in mm (lateral)	Zul. Wellerversatz in mm (axial)	Trägheitsmoment (ca. g cm ²)	Torsionssteife (Nm/rad)	Gewicht (ca. in g)	L	A	G (DIN EN ISO 4762) (ALTE DIN912)	D1/D2	C	F	K
20	0,2	0,25	0,30	11	0,30	17	26	20	M2,5	3...8	3	13	6
30	3,7	0,25	0,30	87	1,8	60	40	30	M4	5...12,7	4,5	20,5	9
40	6,5	0,30	0,30	345	3,7	135	50	40	M5	8...20	5,5	27	11
60	43	0,30	0,30	1850	31	580	83	59	M6	16...30	7,5	41	15
80	105	0,35	0,35	7500	48	1550	104	79	M8	20...45	10	55	20
100	200	0,35	0,35	29000	98	3000	130	99	M12	25...50	12	68	24

B. Material Data from Tensile Tests

Averaged measured data		Input data for ANSYS		
ε_{eng}	$\bar{\sigma}_{eng\ 3-9}$	ε_{tr}	$\varepsilon_{tr,pl}$	σ_{tr}
0.000%	0	0.000%	0.000%	0.0
0.005%	5.1	0.005%	-0.001%	5.1
0.010%	9.0	0.010%	0.000%	9.0
0.015%	12.2	0.015%	0.001%	12.2
0.020%	14.8	0.020%	0.004%	14.8
0.025%	16.8	0.025%	0.006%	16.8
0.030%	18.5	0.030%	0.009%	18.5
0.035%	19.8	0.035%	0.013%	19.8
0.040%	20.9	0.040%	0.017%	20.9
0.045%	21.7	0.045%	0.021%	21.7
0.050%	22.4	0.050%	0.025%	22.4
0.055%	23.1	0.055%	0.029%	23.1
0.060%	23.6	0.060%	0.034%	23.6
0.065%	24.1	0.065%	0.038%	24.1
0.070%	24.5	0.070%	0.043%	24.5
0.075%	24.9	0.075%	0.047%	24.9
0.080%	25.2	0.080%	0.052%	25.2
0.085%	25.5	0.085%	0.057%	25.5
0.090%	25.8	0.090%	0.061%	25.8
0.095%	26.0	0.095%	0.066%	26.0
0.10%	26.2	0.10%	0.071%	26.3
0.11%	26.6	0.11%	0.080%	26.7
0.12%	27.0	0.12%	0.090%	27.0
0.13%	27.3	0.13%	0.099%	27.4
0.14%	27.6	0.14%	0.11%	27.7
0.15%	27.9	0.15%	0.12%	27.9
0.16%	28.1	0.16%	0.13%	28.2
0.17%	28.4	0.17%	0.14%	28.4
0.18%	28.6	0.18%	0.15%	28.7
0.19%	28.8	0.19%	0.16%	28.9
0.20%	29.0	0.20%	0.17%	29.1
0.25%	30.0	0.25%	0.22%	30.0
0.30%	30.8	0.30%	0.27%	30.9
0.35%	31.6	0.35%	0.31%	31.7
0.40%	32.4	0.40%	0.36%	32.5
0.45%	33.2	0.45%	0.41%	33.3
0.50%	33.9	0.50%	0.46%	34.1
0.6%	35.4	0.6%	0.56%	35.6
0.7%	36.9	0.7%	0.66%	37.2
0.8%	38.4	0.8%	0.75%	38.7
0.9%	39.9	0.9%	0.85%	40.2

ε_{eng}	$\bar{\sigma}_{eng\ 3-9}$	ε_{tr}	$\varepsilon_{tr,pl}$	σ_{tr}
1%	41.3	1.0%	0.95%	41.8
2%	55.7	2.0%	1.92%	56.8
3%	69.5	3.0%	2.88%	71.6
4%	82.7	3.9%	3.83%	86.0
5%	95.2	4.9%	4.77%	99.9
6%	106.9	5.8%	5.70%	113.3
7%	117.8	6.8%	6.63%	126.0
8%	127.9	7.7%	7.54%	138.1
9%	137.2	8.6%	8.45%	149.5
10%	145.7	9.5%	9.35%	160.2
11%	153.5	10.4%	10.25%	170.3
12%	160.6	11.3%	11.13%	179.9
13%	167.1	12.2%	12.01%	188.8
14%	172.9	13.1%	12.88%	197.2
15%	178.3	14.0%	13.75%	205.0
16%	183.1	14.8%	14.61%	212.3
17%	187.4	15.7%	15.46%	219.2
18%	191.3	16.6%	16.30%	225.7
19%	194.8	17.4%	17.14%	231.8
20%	197.9	18.2%	17.97%	237.5
21%	200.8	19.1%	18.79%	242.9
22%	203.3	19.9%	19.61%	248.0
23%	205.5	20.7%	20.42%	252.8
24%	207.5	21.5%	21.23%	257.3
25%	209.3	22.3%	22.02%	261.6
26%	210.8	23.1%	22.82%	265.6
27%	212.1	23.9%	23.60%	269.4
28%	213.2	24.7%	24.38%	272.9
29%	214.1	25.5%	25.16%	276.2

C. Detail Views from the Analysis of the planned Gun

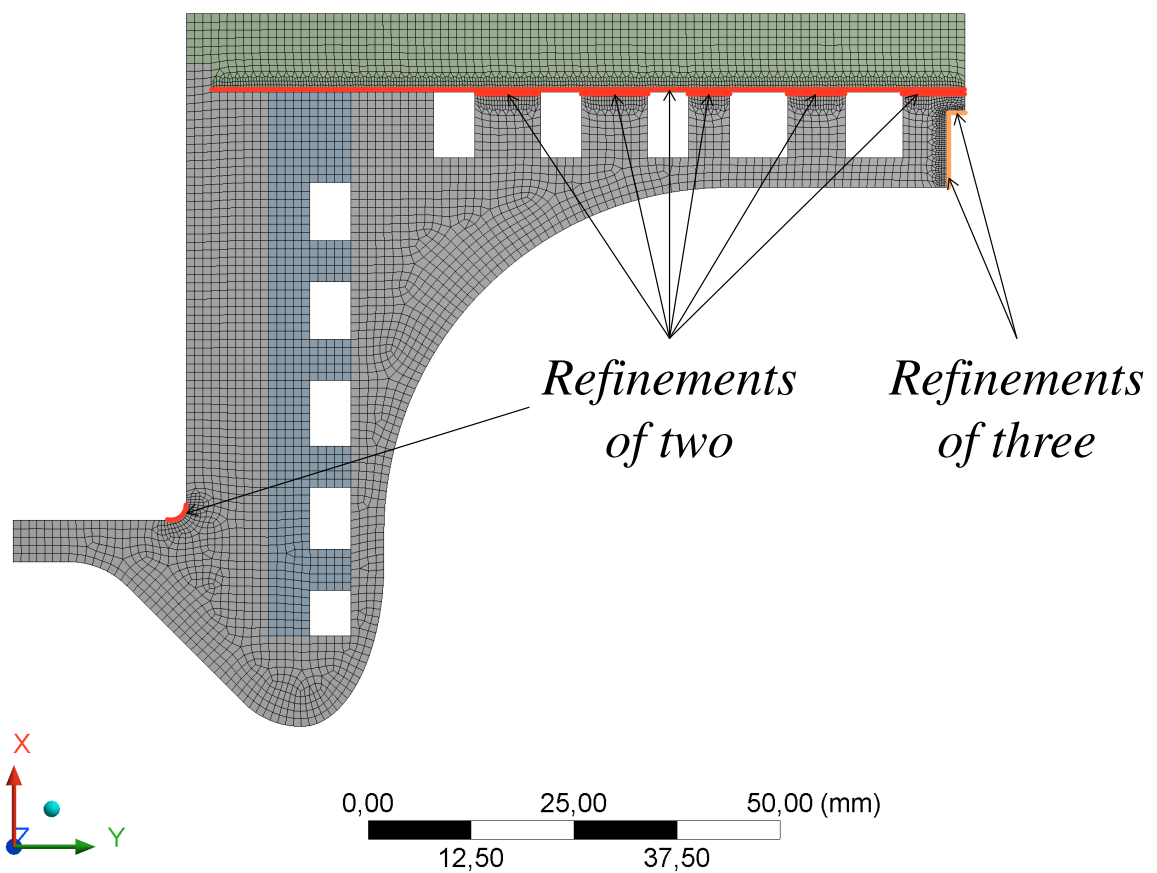


Figure C.1.: Mesh with an element size of 1 mm used for the front end of the gun

Type: Equivalent (von-Mises) Stress
Unit: MPa

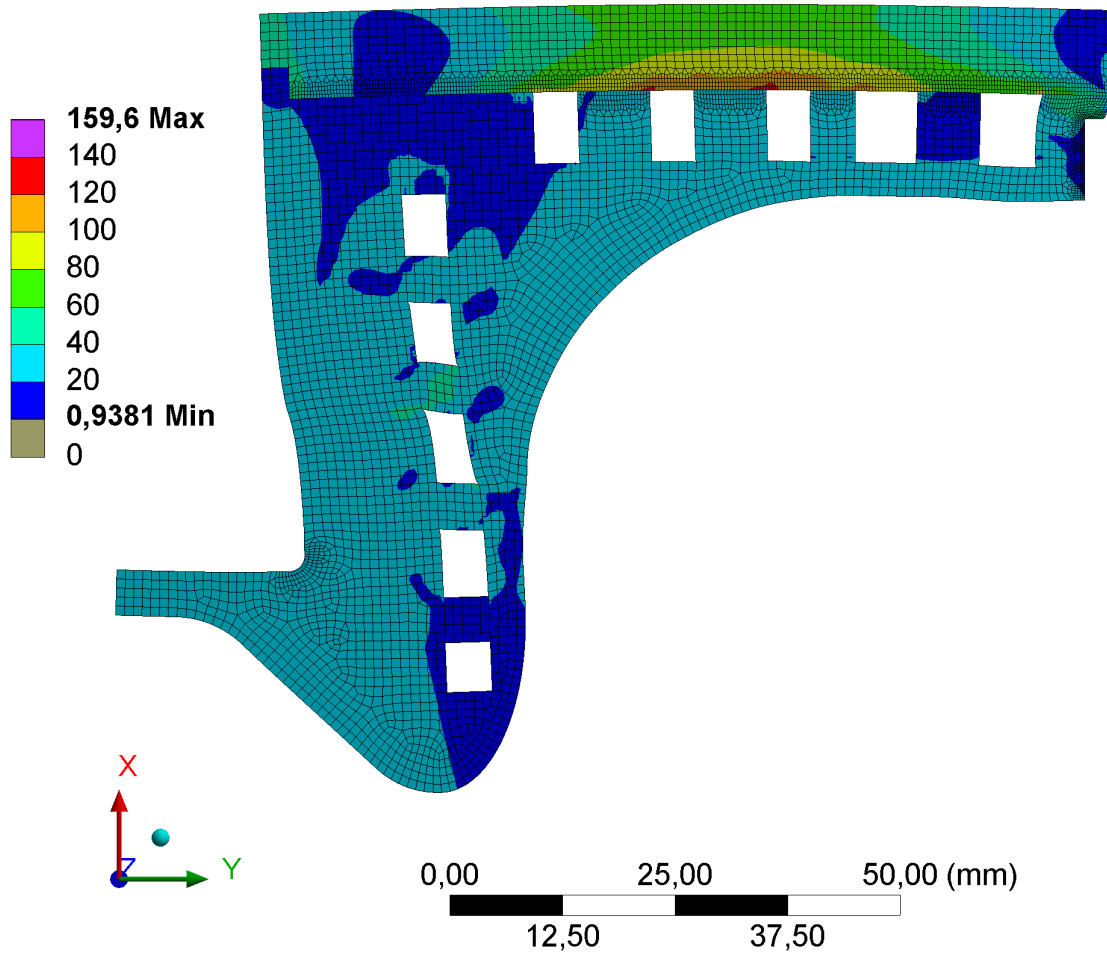


Figure C.2.: Stress distribution at the front end of the gun under a load of 200 kN, calculated with an element size of 1 mm

Type: Equivalent (von-Mises) Stress
Unit: MPa

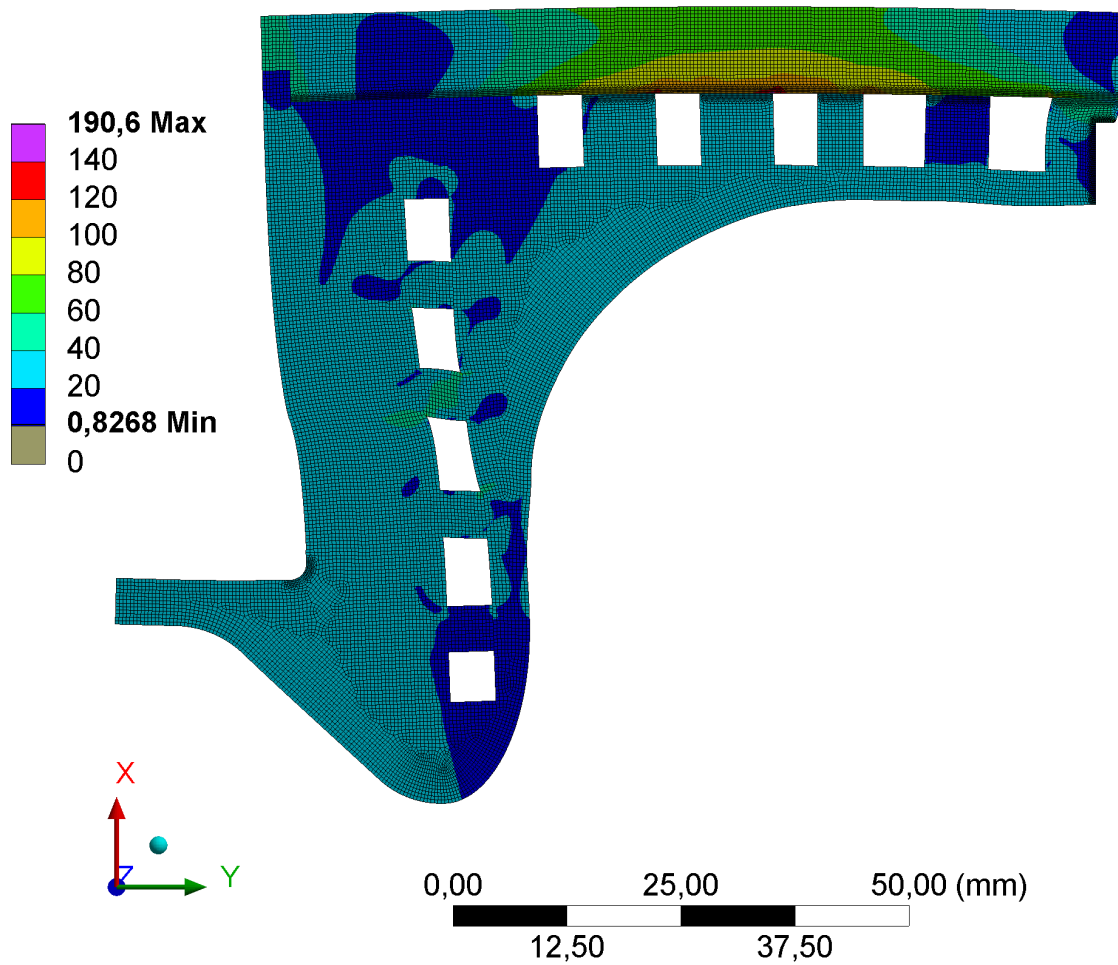


Figure C.3.: Stress distribution at the front end of the gun under a load of 200 kN, calculated with an element size of 0.4 mm

Type: Directional Deformation(Y Axis)
Unit: mm

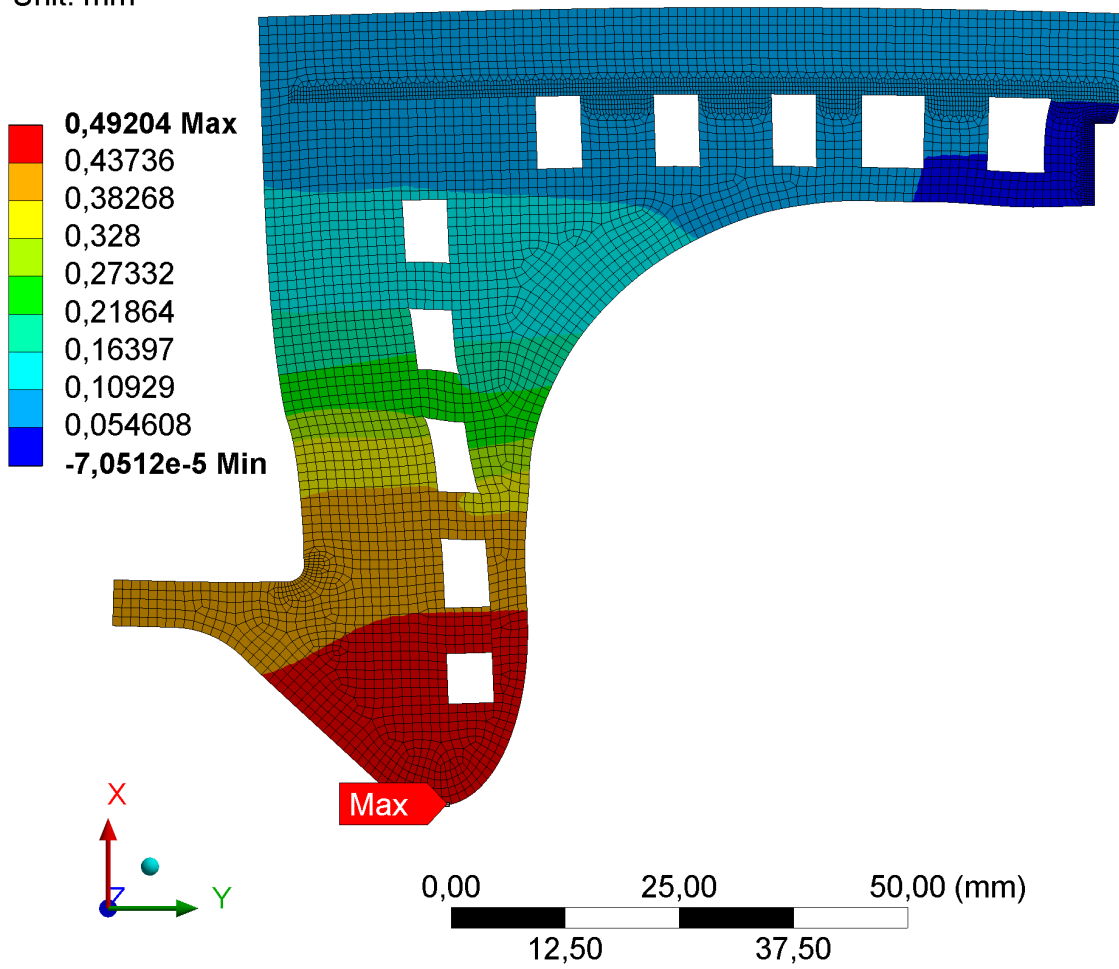


Figure C.4.: Directional deformation of the front end under a load of 200 kN

Type: Directional Deformation(Y Axis)

Unit: mm

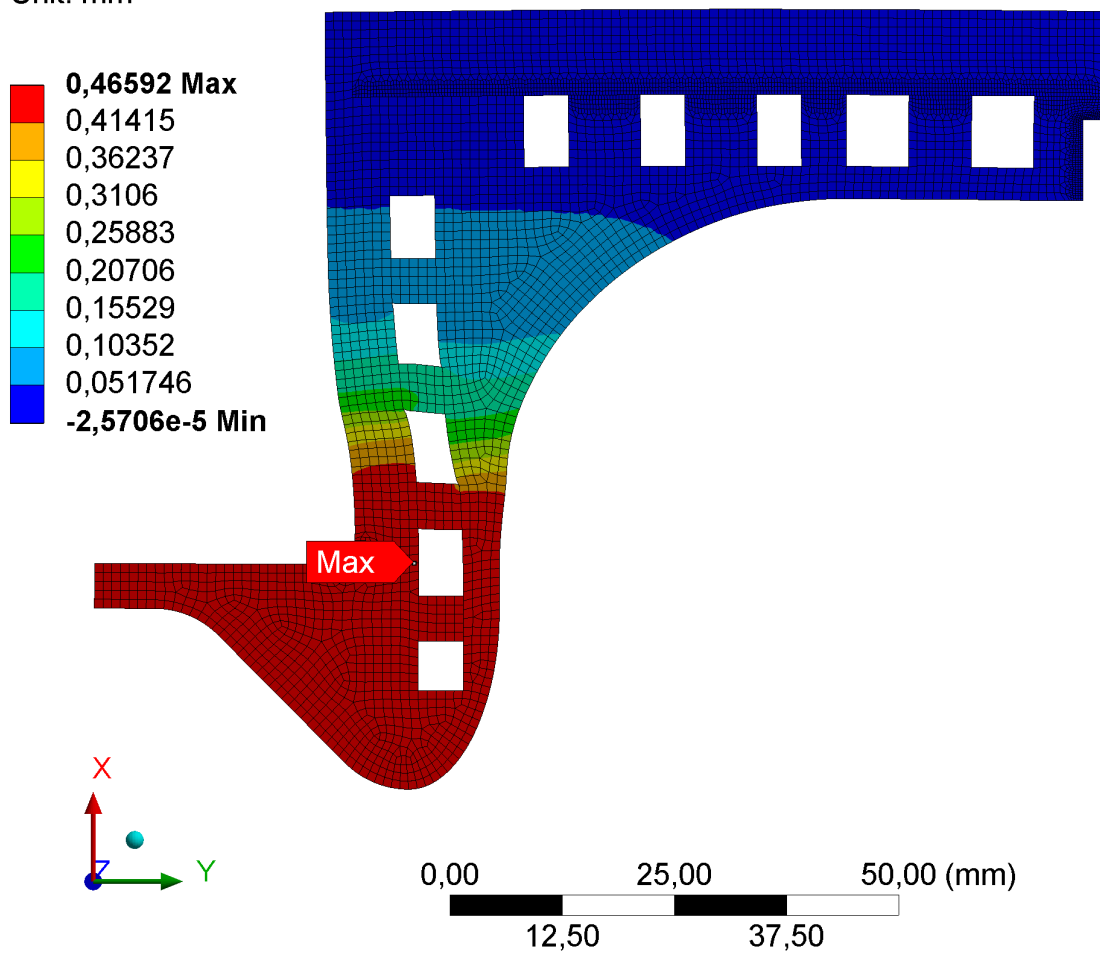


Figure C.5.: Directional deformation of the front end with reduced wall thickness under a load of 140 kN

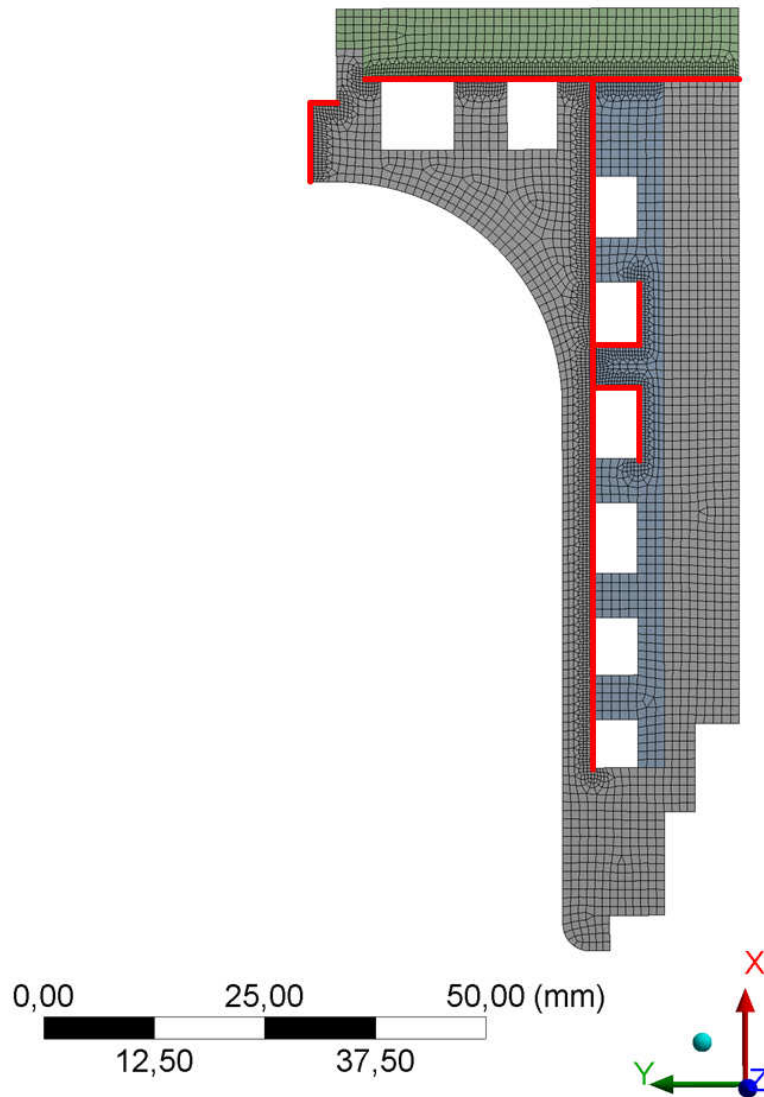


Figure C.6.: Mesh used for the back plane of the gun with an element size of 1 mm and refinements of two in the areas marked in red

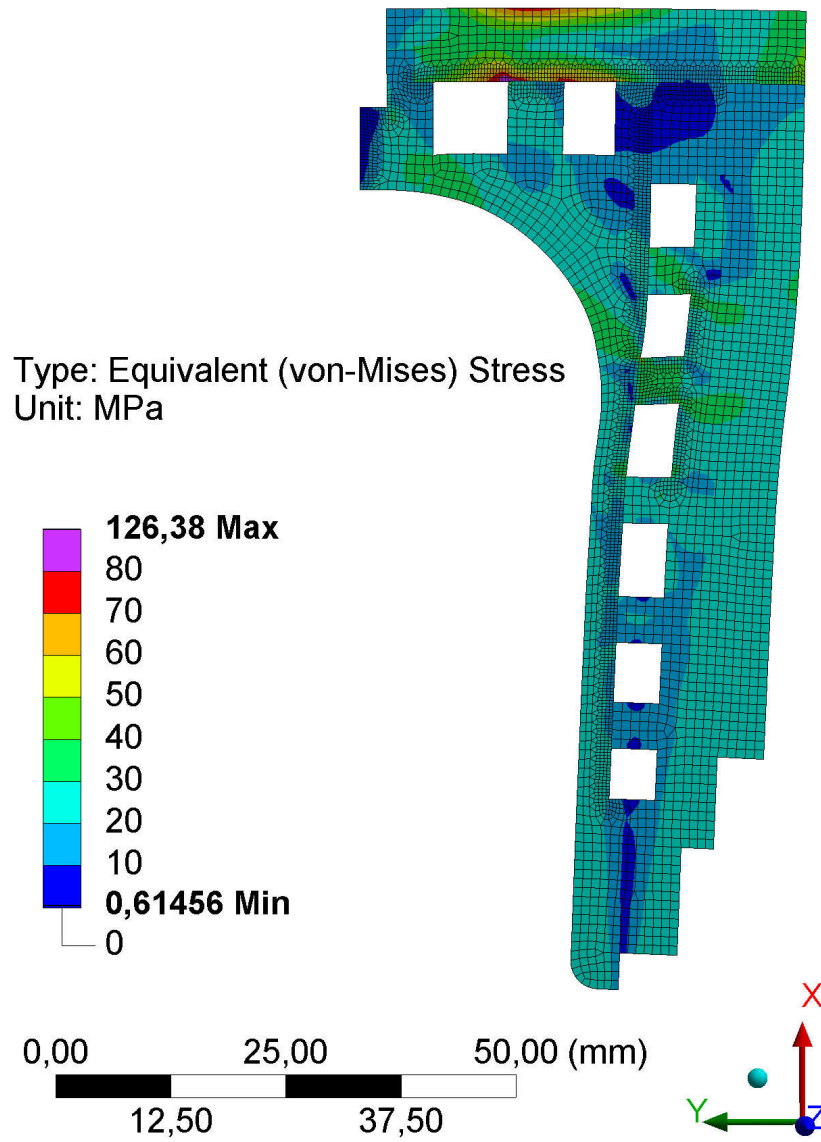


Figure C.7.: Stress distribution at the back plane of the gun under a load of 110 kN

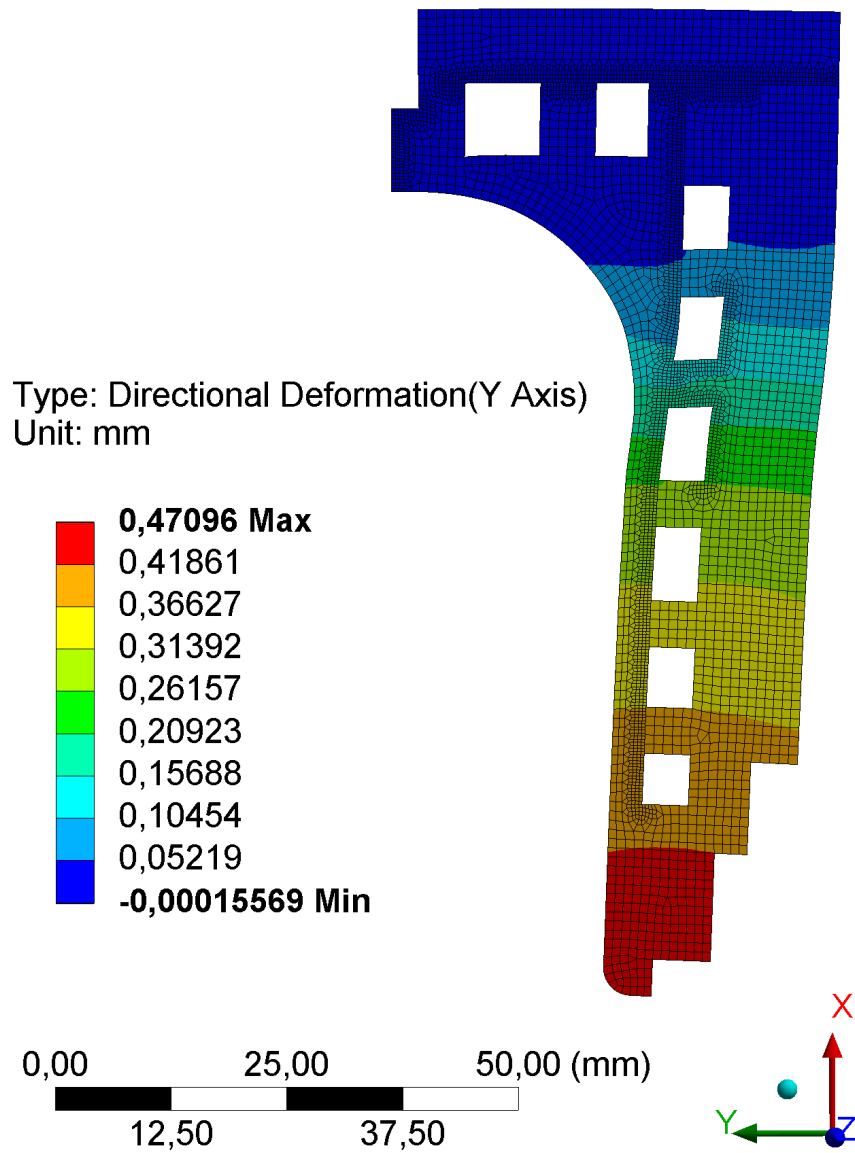


Figure C.8.: Directional deformation of the back plane under a load of 110 kN

Bibliography

- [1] Deutsches Elektronen-Synchrotron DESY. *DESY - Research for the Future*, 2012. Brochure available at http://pr.desy.de/sites2009/site_pr/content/e143921/e143946/teaserboxContent/DESY_Brochure_engl_eng.pdf, visited on 23.10.2014.
- [2] Deutsches Elektronen-Synchrotron DESY. *High Lights*, 2007. Brochure available at http://pr.desy.de/sites2009/site_pr/content/e143921/e143963/teaserboxContent/HighLights_Web_eng.pdf, visited on 23.10.2014.
- [3] Deutsches Elektronen-Synchrotron DESY. *Speed Machines*, 2010. Brochure available at http://pr.desy.de/sites2009/site_pr/content/e143921/e143978/teaserboxContent/SPEED_MACHINES_eng.pdf, visited on 23.10.2014.
- [4] K. Flöttmann. Tuning protocol for Gun 4.3. internal document, 24.07.2012.
- [5] A. Oppelt. Discussion on tuning of electron guns. private communication, 02.06.2014.
- [6] B. Dwersteg, K. Flöttmann, J. Sekutowicz, and Ch. Stolzenburg. RF Gun Design for the TESLA VUV Free Electron Laser. *Nuclear Instruments and Methods in Physics Research Section A: Accelerators, Spectrometers, Detectors and Associated Equipment*, 393(1):93–95, 1997.
- [7] W. Demtröder. *Experimentalphysik 1*. Springer-Verlag, Berlin, Heidelberg, 4th edition, 2006.
- [8] Deutsches Kupferinstitut. *Data sheet for Cu-OFE*, 2005. available at http://www.kupferinstitut.de/fileadmin/user_upload/kupferinstitut.de/de/Documents/Shop/Verlag/Downloads/Werkstoffe/Datenblaetter/Kupfer/Cu-OFE.pdf, visited on 23.09.2014.
- [9] ÜV Überlastschutz u. Verbindungssysteme GmbH. *Technical data sheet for flexible coupling type 300-40*. available at <http://www.uev-gmbh.de/style/data/pdf/uev-gmbh-de-d-ty300.pdf>, visited on 04.11.2014.

- [10] Lineartechnik Korb GmbH. *Technical data sheet for spindle gear SHG-MJ3-L*. available at <http://www.lineartechnik-korb.com>, visited on 04.11.2014.
- [11] DIN EN ISO 6892-1:2009-12. *Metallic materials - Tensile testing - Part 1: Method of testing at room temperature*, 2009.
- [12] DIN EN 10002-1:1991-04. *Metallic materials - Tensile testing - Part 1: Method of testing*, 1991.
- [13] Beuth Verlag GmbH. *Modification note for DIN EN ISO 6892-1:2009-12*. available at <http://www.beuth.de/de/norm/din-en-iso-6892-1/110975410>, visited on 17.10.2014.
- [14] DIN 50125:2009-07. *Testing of metallic materials - Tensile test pieces*, 2009.
- [15] W. Weißbach. *Werkstoffkunde und Werkstoffprüfung*. Vieweg Verlag, Braunschweig Wiesbaden, 13th edition, 2000.
- [16] E. Greven and W. Magin. *Werkstoffkunde und Werkstoffprüfung für technische Berufe*. Verlag Handwerk und Technik, Hamburg, 17th edition, 2012.
- [17] D. Roylance. Stress-strain curves. *Massachusetts Institute of Technology study, Cambridge*, 2001. available at <http://ocw.mit.edu/courses/materials-science-and-engineering/3-11-mechanics-of-materials-fall-1999/modules/ss.pdf>, visited on 23.09.2014.
- [18] R. C. Hibbeler. *Technische Mechanik 2 - Festigkeitslehre*. Pearson Studium, München, 5th edition, 2006.
- [19] ANSYS inc. *Introduction to Structural Nonlinearities; Lecture 4 - Rate Independent Plasticity*, 2014. Training material available at <https://support.ansys.com/portal/site/AnsysCustomerPortal>, visited on 07.11.2014.
- [20] A. C. Reardon. *Metallurgy for the Non-metallurgist*. ASM International, Ohio, 2nd edition, 2011.
- [21] K. Jousten. *Wutz Handbuch Vakuumtechnik*. Vieweg + Teubner Verlag, Wiesbaden, 10th edition, 2010.
- [22] D. Liebertz. Brazing process of electron guns at DESY. private communication, 26.06.2014.
- [23] ANSYS Academic Research, Release 15. *Help System, Element library*. ANSYS inc.

- [24] ME-Messsysteme GmbH. *Technical data sheet for force sensor KM38*. available at <http://www.me-systeme.de/de/datasheets/km38.pdf>, visited on 12.06.2014.
- [25] Keysight Technologies Inc. *Technical data sheet for data acquisition unit 34970A and multiplexer plug-in 34901A*. available at <http://literature.cdn.keysight.com/litweb/pdf/5965-5290EN.pdf>, visited on 21.08.2014.
- [26] Dr. Johannes Heidenhain GmbH. *Technical data sheet for incremental length gauge ST 1288*. available at http://www.heidenhain.de/de_EN/php/documentation-information/brochures/popup/media/media/file/view/file-0441/file.pdf, visited on 21.08.2014.
- [27] Dr. Johannes Heidenhain GmbH. *Technical data sheet for evaluation unit type ND 2100G GAGE-CHECK*. available at http://www.heidenhain.com/fileadmin/pdb/media/img/1102714-20_Evaluation_Electronics.pdf, visited on 21.08.2014.
- [28] Y.V.R.K. Prasad and S. Sasidhara. *Hot working guide: a compendium of processing maps*. ASM international, Ohio, 1997.

Statutory Declaration

I, Sebastian Philipp, hereby declare that I have written this thesis independently, unless where clearly stated otherwise. I have used only the sources, the data and the support that I have clearly mentioned. This thesis has not been submitted for conferral of degree elsewhere.

Date/Signature